An empirical algorithm to map perennial firn aquifers and ice slabs within the Greenland Ice Sheet using satellite L-band microwave radiometry

Julie Z. Miller[1,2], Riley Culberg[3], David G. Long[4], Christopher A. Shuman[5], Dustin M. Schroeder[3,6], Mary J. Brodzik[1,7]

[1]Cooperative Institute for Research in Environmental Sciences, University of Colorado, Boulder, Colorado, USA

[2]Earth Science and Observation Center, University of Colorado, Boulder, Colorado, USA

[3]Department of Electrical Engineering, Stanford University, Stanford, California, USA

[4]Department of Electrical and Computer Engineering, Brigham Young University, Provo, Utah, USA

[5]University of Maryland, Baltimore County, Joint Center for Earth Systems Technology at Code 615, Cryospheric Sciences Laboratory NASA Goddard Space Flight Center, Greenbelt, Maryland, USA

[6]Department of Geophysics, Stanford University, Stanford, CA, USA

[7]National Snow and Ice Data Center, University of Colorado, Boulder, Colorado, USA

Correspondence to: jzmiller.research@gmail.com

Abstract

Perennial firn aquifers are subsurface meltwater reservoirs consisting of a meters-thick water-saturated firn layer that can form on spatial scales as large as tens of kilometers. They have been observed within the percolation facies of glaciated regions experiencing intense seasonal surface melting and high snow accumulation. Widespread perennial firn aquifers have been identified within the Greenland Ice Sheet (GrIS) via field expeditions, airborne ice-penetrating radar surveys, and satellite microwave sensors. In contrast, ice slabs are nearly-continuous ice layers that can also form on spatial scales as large as tens of kilometers as a result of surface and subsurface water-saturated snow and firn layers sequentially refreezing following multiple melting seasons. They have been observed within the percolation facies of glaciated regions experiencing intense seasonal surface melting, but in areas where snow accumulation is at least 25% lower as compared to perennial firn aquifer areas. Widespread ice slabs have recently been identified within the GrIS via field expeditions and airborne ice-penetrating radar surveys, specifically in areas where perennial firn aquifers typically do not form. However, ice slabs have yet to be identified from space. Together, these two ice sheet features represent distinct, but related, sub-facies within the broader percolation facies of the GrIS that can be defined primarily by differences in snow accumulation, which influences the englacial hydrology and thermal characteristics of firn layers at depth.

Here, for the first time, we use enhanced-resolution vertically-polarized L-band brightness temperature (T_V^B) imagery (2015-2019) generated using observations collected over the GrIS by NASA's Soil Moisture Active Passive (SMAP) satellite to map perennial firn aquifer and ice slab areas together as a continuous englacial hydrological system. We use an empirical algorithm previously developed to map the extent of Greenland's perennial firn aquifers via fitting exponentially decreasing temporal L-band signatures to a set of sigmoidal curves. This algorithm is recalibrated to also map the extent of ice slab areas using airborne ice-penetrating radar surveys collected by NASA's Operation Ice Bridge (OIB) campaigns (2010-2017). Our SMAP-derived maps

show that between 2015 and 2019, perennial firn aquifer areas extended over 64,000 km², and ice slab areas extended over 76,000 km². Combined together, these sub-facies are the equivalent of 24% of the percolation facies of the GrIS. As Greenland's climate continues to warm, seasonal surface melting will increase in extent, intensity, and duration. Quantifying the possible rapid expansion of these sub-facies using satellite L-band microwave radiometry has significant implications for understanding ice sheet-wide variability in englacial firn hydrology that may drive meltwater-induced hydrofracturing and accelerated ice flow as well as high-elevation meltwater runoff that can impact the mass balance and stability of the GrIS.

1   Introduction

The recent launches of several satellite L-band microwave radiometry missions by NASA (Aquarius mission, Levine, et al., 2007; Soil Moisture Active Passive (SMAP) mission, Entekhabi et al., 2010) and ESA (Soil Moisture and Ocean Salinity (SMOS), Kerr et al., 2010) have provided a new Earth-observation tool capable of detecting meltwater stored tens of meters to kilometers beneath the ice sheet surface. Jezek et al. (2015) recently demonstrated that in the high-elevation (3500 m a.s.l.) dry snow facies of the Antarctic Ice Sheet, meltwater stored in subglacial Lake Vostok can be detected as deep as 4 km beneath the ice sheet surface. Subglacial lakes represent radiometrically cold subsurface meltwater reservoirs. Upwelling L-band emission from the radiometrically warm bedrock underlying the subglacial lakes is effectively blocked by high reflectivity and attenuation at the interface between the bedrock and the overlying lake bottom. This results in a lower observed microwave brightness temperature (T^B) at the ice sheet surface as compared to other dry snow facies areas where bedrock contributes to L-band emission depth-integrated over the entire ice sheet thickness.

Similar to subglacial lakes, perennial firn aquifers also represent radiometrically cold subsurface meltwater reservoirs (Miller et al., 2020) consisting of a 4-25 m thick water-saturated firn layer (Koenig et al., 2014; Montgomery et al., 2017; Chu et al., 2018) that can form on spatial scales as large as tens of kilometers (Forster et al., 2014). Perennial firn aquifers have been identified via field expeditions (Forster et al., 2014), airborne ice-penetrating radar surveys (Miège et al., 2016), and satellite microwave sensors (Brangers et al., 2020; Miller et al., 2020) in the lower-elevation (<2000 m a.s.l.) percolation facies of the Greenland Ice Sheet (GrIS) at depths from between 1 m and 40 m beneath the ice sheet surface. They exist in areas that experience intense seasonal surface melting and rain (>650 mm w.e. yr⁻¹) during the melting season and high snow accumulation (>800 mm w.e. yr⁻¹) during the freezing season (Forster et al., 2014). High snow accumulation in perennial firn aquifer areas thermally insulates water-saturated firn layers from the cold atmosphere allowing seasonal meltwater to be stored in liquid form year-round if the overlying seasonal snow layer is sufficiently thick (Kuipers Munneke et al., 2014). Koenig et al. (2014) estimated that the volumetric fraction of meltwater stored within the pore space of Greenland's perennial firn aquifers just prior to melt onset ranges from between 10% and 25%, which limits the upward propagation of electromagnetic energy from greater depths within the ice sheet. Large volumetric fractions of meltwater within the firn pore space results in high reflectivity and attenuation at the interface between water-saturated

firn layers and the overlying refrozen firn layers, and between glacial ice or an impermeable layer and the overlying water-saturated firn layers. Upwelling L-band emission from deeper glacial ice and the underlying bedrock is effectively blocked.

While perennial firn aquifers are radiometrically cold, the slow refreezing of deeper firn layers saturated with large volumetric fractions of meltwater represents a significant source of latent heat that is continuously released throughout the freezing season. Refreezing of seasonal meltwater by the descending winter cold wave (Pfeffer et al., 1991), and the subsequent formation of embedded ice structures (i.e., horizontally-oriented ice layers and ice lenses, and vertically-oriented ice pipes; Benson et al., 1960; Humphrey et al., 2012; Harper et al., 2012) within the upper snow and firn layers represents a secondary source of latent heat. These heat sources help maintain meltwater at depth. Perennial firn aquifer areas are radiometrically warmer than other percolation facies areas where the single source of latent heat is via refreezing of seasonal meltwater. This results in a higher observed T^B at the ice sheet surface during the freezing season as compared to other percolation facies areas where seasonal meltwater is fully refrozen and stored exclusively as embedded ice.

Recently, mapping the extent of Greenland's perennial firn aquifers from space was demonstrated using satellite L-band microwave radiometry (Miller et al., 2020). Exponentially decreasing temporal L-band signatures observed in enhanced-resolution vertically-polarized L-band brightness temperature (T_V^B) imagery (2015-2016) generated using observations collected over the GrIS by the microwave radiometer on NASA's SMAP satellite (Long et al., 2019) were correlated with a single year of perennial firn aquifer detections (Miège et al. 2016). These detections were identified via the Center for Remote Sensing of Ice Sheets (CReSIS) Multi-Channel Coherent Radar Depth Sounder (MCoRDS) flown by NASA's Operation Ice Bridge (OIB) campaigns (Rodriguez-Morales et al, 2014). An empirical algorithm to map extent was developed by fitting temporal L-band signatures to a set of sigmoidal curves derived from the continuous logistic model.

The relationship between the radiometric, and thus the physical, temperature of perennial firn aquifer areas, as compared to other percolation facies areas, forms the basis of the empirical algorithm. Miller et al. (2020) hypothesized that the dominant control on the relatively slow exponential rate of T^B decrease over perennial firn aquifer areas is physical temperature versus depth. L-band emission from the radiometrically warm upper snow and firn layers decreases during the freezing season as embedded ice structures slowly refreeze at increased depths below the ice sheet surface. In the percolation facies, refreezing of seasonal meltwater results in the formation of an intricate network of embedded ice structures that are large (10-100 cm long, 10-20 cm wide; Jezek et al., 1994) relative to the L-band wavelength (21 cm). Embedded ice structures induce strong volume scattering (Rignot et al., 1993; Rignot 1995) that decreases T^B (Zwally, 1977; Swift et al. 1985; Jezek et al., 2018).

Ice slabs are 1-16 m thick nearly-continuous ice layers that that can form on spatial scales as large as tens of kilometers as a result of surface and subsurface water-saturated snow and firn layers sequentially refreezing following multiple melting seasons (Machguth et al., 2016; MacFerrin et al., 2019). Over time,

115   they become dense low-permeability solid-ice layers overlying deeper permeable firn layers. Ice slabs have
116   been identified via field expeditions and airborne ice-penetrating radar surveys in the lower-elevation
117   (<2000 m a.s.l.) percolation facies of the GrIS at depths from between 1 m and 20 m beneath the ice sheet
118   surface (MacFerrin et al., 2019). They exist in areas that experience intense seasonal surface melting and
119   rain (excess melt of 266-573 mm w.e. yr−1, see MacFerrin et al., (2019) for a description) during the melting
120   season, and lower snow accumulation (<572+/-32 mm w.e. yr−1) during the freezing season as compared
121   to perennial firn aquifer areas (MacFerrin et al., 2019). Lower snow accumulation in ice slab areas results
122   in a seasonal snow layer that is insufficiently thick to thermally insulate water-saturated firn layers and
123   seasonal meltwater is instead stored as embedded ice. Refreezing of seasonal meltwater by the
124   descending winter cold wave, and the subsequent formation of ice slabs as well as other embedded ice
125   structures within the upper snow and firn layers is the single source of latent heat. While ice slab areas are
126   radiometrically warmer than other percolation facies areas with a lower volumetric fraction of embedded
127   ice, they are radiometrically colder than perennial firn aquifer areas. This results in typically higher observed
128   T^B at the ice sheet surface during the freezing season in ice slab areas, as compared to other percolation
129   facies areas, however, typically lower observed T^B as compared to perennial firn aquifer areas. Similar to
130   temporal L-band signatures over perennial firn aquifer areas, temporal L-band signatures over ice slab
131   areas are exponentially decreasing during the freezing season, however, the rate of T^B decrease is slightly
132   more rapid.
133   In this study, we exploit the observed sensitivity of L-band emission to differences in the depth- and
134   time-integrated dielectric and geophysical properties of the percolation facies of the GrIS to map perennial
135   firn aquifer and ice slab areas together as a continuous englacial firn hydrological system using satellite L-
136   band microwave radiometry.

2   Methods

138   We adapt our previously developed empirical algorithm to map the extent of Greenland's perennial firn
139   aquifers (Miller et al., 2020) using a multi-year calibration technique. We use enhanced-resolution L-band
140   T_V^B imagery (2015-2019) generated using observations collected over the GrIS by the microwave
141   radiometer on NASA's SMAP satellite (Long et al., 2019) and airborne ice-penetrating radar surveys
142   collected by NASA's OIB campaigns (Rodriguez-Morales et al, 2014). First, we correlate: (1) a 'firn
143   saturation' parameter derived from a simple two-layer L-band brightness temperature model (2) maximum
144   and (3) minimum T_V^B values, and (4) exponentially decreasing temporal L-band signatures, with five years
145   of perennial firn aquifer detections (2010-2014) identified via the CReSIS Accumulation Radar (AR) (Miège
146   et al. 2016), and three years of additional detections (2015-2017) more recently identified via MCoRDS
147   (Miller et al., 2020). Next, we extend our empirical algorithm to map the extent of ice slab areas. We
148   correlate the SMAP-derived parameters with five years of ice slab detections (2010-2014) recently identified
149   via AR (MacFerrin et al., 2019). Finally, we re-calibrate our empirical model to map the extent of perennial
150   firn aquifer and ice slab areas over the percolation facies. Interannual variability in extent is not resolved in

151   this study, however, it will be explored further in future work.

2.1   SMAP Enhanced-Resolution L-band T^B Imagery

153   The key science objectives of NASA's SMAP mission (https://smap.jpl.nasa.gov/) are to map terrestrial soil
154   moisture and freeze/thaw state over Earth's land surfaces from space. However, the global L-band T^B
155   observations collected by the SMAP satellite also have cryospheric applications. Mapping perennial firn
156   aquifer and ice slab areas over Earth's polar ice sheets represents an interesting analog and an innovative
157   extension of the SMAP mission's science objectives. The SMAP satellite was launched 31 January 2015
158   and carries a microwave radiometer that operates at an L-band frequency of 1.41 GHz (Enkentabi et al.,
159   2010). It is currently collecting observations of vertically and horizontally-polarized T^B over Greenland. The
160   surface incidence angle is 40°, and the radiometric accuracy is approximately 1.3 K (Piepmeier et al., 2017).

161   The Scatterometer Image Reconstruction (SIR) algorithm was originally developed to reconstruct
162   coarse resolution satellite radar scatterometry imagery on a higher spatial resolution grid (Long et al., 1993;
163   Early and Long, 2001). The SIR algorithm has been adapted for coarse resolution satellite microwave
164   radiometry imagery (Long and Daum, 1998; Long and Brodzik, 2016; Long et al., 2019). The microwave
165   radiometer form of the SIR algorithm (rSIR) uses the measurement response function (MRF) for each
166   observation, which is a smeared version of the antenna pattern. Using the overlapping MRFs, the rSIR
167   algorithm reconstructs T^B from the spatially filtered low-resolution sampling provided by the observations.
168   In effect, it generates an MRF-deconvolved T^B image. Combining multiple orbital passes increases the
169   sampling density, which improves both the accuracy and resolution of the SMAP enhanced-resolution T^B
170   imagery (Long et al., 2019).

171   Over Greenland, the rSIR algorithm combines satellite orbital passes that occur between 8 a.m.
172   and 4 p.m. local time-of-day to reconstruct SMAP enhanced-resolution T^B imagery twice-daily (i.e., morning
173   and evening orbital pass interval, respectively). T^B imagery is projected on a Northern Hemisphere (NH)
174   Equal-Area Scalable Earth Grid (EASE-Grid 2.0; Brodzik et al., 2012) at a 3.125 km rSIR grid cell spacing
175   (e.g., Fig. 1). The effective resolution for each grid cell is dependent on the number of observations used
176   in the rSIR reconstruction and is coarser than the rSIR grid cell spacing. While the effective resolution of
177   conventionally processed SMAP T^B imagery posted on a 25 km grid is approximately 30 km (e.g., Fig. 1a),
178   the effective resolution of SMAP enhanced-resolution T^B imagery posted on a 3.125 km grid is
179   approximately 18 km (e.g., Fig. 1b), an improvement of 60% (Long et al., 2020).

180   As previously noted, for our analysis of the percolation facies we use SMAP enhanced-resolution
181   T_V^B imagery over the GrIS. Compared to the horizontally-polarized channel, the vertically-polarized channel
182   exhibits decreased sensitivity to variability in the volumetric fraction of meltwater, which is attributed to
183   reflection coefficient differences between channels (Miller et al., 2020). Using the vertically polarized
184   channel also results in a reduced chi-squared error statistic when fitting T_V^B time series to the sigmoid
185   function (Section 2.3.4). We construct T_V^B imagery that alternate morning and evening orbital pass
186   observations annually, beginning and ending just prior to melt onset. The Greenland Ice Mapping Project

187   (GIMP) Land Ice and Ocean Classification Mask and Digital Elevation Model (Howat et al., 2014) are
188   projected on the NH EASE-Grid 2.0 at a 3.125 km rSIR grid cell spacing. The derived ice mask includes
189   the Greenland Ice Sheet and the peripheral ice caps, including Maniitsoq and Flade Isblink.T_V^B imagery
190   between 1 April 2015 and 31 March 2019 are ice -masked, and an elevation for each rSIR grid cell is
191   calculated.

2.2   Airborne Ice-Penetrating Radar Surveys

193   AR and MCoRDS (Rodriguez-Morales et al, 2014) were flown over the GrIS on a P-3 aircraft in
194   April and May between 2010 and 2017. The AR instrument operates at a center frequency of 750 MHz with
195   a bandwidth of 300 MHz, resulting in a range resolution in firn of 0.53 m (Lewis et al., 2015). The collected
196   data have an along-track resolution of approximately 30 m with 15 m spacing between traces in the final
197   processed radargrams. At a nominal flight altitude of 500 m above the ice sheet surface, the cross-track
198   resolution varies between 20 m for a smooth surface, to 54 m for a rough surface with no appreciable
199   layover. The MCoRDS instrument operated at three different frequency configurations: (1) a center
200   frequency of 195 MHz with a bandwidth of 30 MHz (2010-2014, 2017, 2018), (2) a center frequency of 315
201   MHz with a band width of 270 MHz (2015), and (3) a center frequency of 300 MHz with a bandwidth of 300
202   MHz (2016). The vertical range resolution in firn for each of these frequency configurations is 5.3 m, 0.59
203   m, and 0.53m, respectively (CReSIS, 2016). The collected data have an along-track resolution of
204   approximately 25 m with 14 m spacing between traces in the final processed radargrams. At the same
205   nominal flight altitude of 500 m, the cross-track resolution varies between 40 m for a smooth surface in the
206   highest bandwidth configuration, to 175 m for a rough surface with no appreciable layover in the lowest
207   bandwidth configuration.

208   The multi-year calibration technique uses perennial firn aquifer detections previously identified
209   along OIB flight lines via AR (2010-2014) and MCoRDS (2015-2017) radargram profiles and the
210   methodology described in Miège et al. (2016). Bright lower reflectors that undulate with the local
211   topographic gradient underneath which reflectors are absent in the percolation facies are interpreted as the
212   upper surface of meltwater stored within perennial firn aquifers (e.g., Fig. 3a). The large dielectric contrast
213   between refrozen and water-saturated firn layers results in high reflectivity at the interface. However, the
214   presence of meltwater increases attenuation, limiting the downward propagation of electromagnetic energy
215   through the water-saturated firn layer. The total number of AR derived perennial firn aquifer detections is
216   325,000, corresponding to a total extent of 98 km^2. The analysis assumes a smooth surface, which is typical
217   of much of the percolation facies, and a grid cell size of 15 m x 20 m. The total number of MCoRDS-derived
218   perennial firn aquifer detections is 142,000, corresponding to a total extent of 80 km^2. This analysis also
219   assumes a smooth surface, and a grid cell size of 14 m x 40 m. The combined total number of grid cells
220   (467,000) and total extent (178 km^2) is significantly larger than the total number of MCoRDS-derived grid
221   cells (78,000) and total extent (44 km^2) calculated for 2016 (Miller et al., 2020). Perennial firn aquifer
222   detections are mapped in north western, southern, and south and central eastern Greenland as well as the

223   Maniitsoq and Flade Isblink Ice Caps (Figs. 1c; 2a). We project AR- and MCoRDS-derived perennial firn

224   aquifer detections on the NH EASE-Grid 2.0 at an rSIR grid cell spacing of 3.125 km. Each rSIR grid cell

225   has an extent of approximately 10 km^2. The total number of rSIR grid cells with at least one perennial firn

226   aquifer detection is 800, corresponding to a total extent of 8000 km^2. However, given the limited AR and

227   MCoRDS grid cell coverage, less than 1% of the rSIR grid cell extent has airborne ice-penetrating radar

228   survey coverage. As compared to the total number of MCoRDS-derived perennial firn aquifer detections

229   (780) calculated for 2016 (Miller et al., 2020), the total number of rSIR grid cells with at least one detection

230   is only increased by 20 for the multi-year calibration technique, corresponding to an increased total extent

231   of 200 km^2.

232   We also use ice slab detections previously identified along OIB flight lines via AR (2010-2014)

233   radargram profiles and the methodology described in MacFerrin et al. (2019) in the multi-year calibration

234   technique. Thick dark surface-parallel regions of low-reflectivity in the percolation facies are interpreted as

235   ice slabs (e.g., Fig. 3b). The large dielectric contrast between ice slabs and the overlying and underlying

236   snow and firn layers results in high reflectivity at the interfaces. However, electromagnetic energy is not

237   scattered or absorbed within the homogeneous ice slab, it instead propagates downward through the layer

238   and into the deeper firn layers. The total number of AR-derived ice slab detections is 505,000,

239   corresponding to a total extent of 283 km^2. Ice slab detections are mapped in western, central and north

240   eastern, and northern Greenland as well as the Flade Isblink Ice Cap (Figs. 1c; 2b). We project the AR-

241   derived ice slab detections on the NH EASE-Grid 2.0 at an rSIR grid cell spacing of 3.125 km. The total

242   number of rSIR grid cells with at least one ice slab detection is 2000, corresponding to a total extent of

243   20,000 km^2. However, less than 2% of the rSIR grid cell extent has airborne ice-penetrating radar survey

244   coverage.

245   An advantage of the multi-year calibration technique as compared to the single-coincident year

246   calibration technique (Miller et al., 2020) is that it increases the number of rSIR grid cells that can be

247   assessed. It also provides repeat targets that can account for variability in the depth- and time-integrated

248   dielectric and geophysical properties that influence the radiometric temperature in stable perennial firn

249   aquifer and ice slab areas. Uncertainty is introduced by correlating the SMAP-derived parameters with AR-

250   and MCoRDS-derived detections that are not coincident in time. The multi-year calibration technique

251   assumes the extent of each area remains stable, which is not necessarily the case as climate extremes

252   (Cullather et al., 2020) can influence each of these sub-facies. The assumption of stability neglects

253   boundary transitions in the extent of perennial firn aquifer areas associated with refreezing of shallow water-

254   saturated firn layers, englacial drainage of meltwater into crevasses at the periphery (Poinar et al., 2017;

255   Poinar et al, 2019), and transient upslope expansion (Montgomery et al., 2017). Once formed, ice slabs are

256   essentially permanent features within the upper snow and firn layers of the percolation facies until they are

257   compressed into glacial ice. However, they may transition into superimposed ice at the lower boundary of

258   ice slab areas or rapidly expand upslope, particularly following extreme melting seasons (MacFerrin et al.,

259   2019). Thus, we simply consider our mapped extent a high-probability area for the preferential formation of

260 each of these sub-facies, with continued presence dependent on seasonal surface melting and snow
261 accumulation in subsequent years.

262   Annual perennial firn aquifer and ice slab detections that may introduce significant uncertainty into
263 the multi-year calibration technique include those following the 2010 melting season, which was
264 exceptionally long (Tedesco et al., 2011), the anomalous 2012 melting season, during which seasonal
265 surface melting extended across 99% of the GrIS (Nghiem et al., 2012), and the 2015 melting season,
266 which was especially intense in western and northern Greenland (Tedesco et al., 2016). Following these
267 extreme melting seasons, significant changes in the dielectric and geophysical properties likely occurred
268 across large portions of the GrIS, including perennial firn aquifer recharging resulting in increases in
269 meltwater volume and decreases in the depth to the upper surface of stored meltwater. The upper snow
270 and firn layers of the dry snow facies and percolation facies were also saturated with relatively large
271 volumetric fractions of meltwater as compared to the negligible to limited volumetric fractions of meltwater
272 that percolates during more typical seasonal surface melting on the GrIS.

273   Seasonal meltwater was refrozen into spatially coherent melt layers following the 2010 and 2012
274 melting seasons (Culberg et al., 2021) as well as more recently following the 2015, and 2018 melting
275 seasons identified as part of the temporal L-band signature analysis in this study (Section 2.3.1). As
276 compared to ice slabs, which are dense low-permeability solid-ice layers, spatially coherent melt layers are
277 a network of embedded ice structures primarily consisting of discontinuous horizontally-oriented ice layers
278 and ice lenses sparsely connected via vertical-oriented ice pipes (Culberg et al., 2021). Spatially coherent
279 melt layers are relatively thin (0.2 cm-2 m) and can rapidly form across the high-elevation (up to 3200 m
280 a.s.l.) dry snow facies at depths of less than 1 m beneath the ice sheet surface following a single extreme
281 melting season. They can further merge together into thicker solid-ice layers following multiple extreme
282 melting seasons. Spatially coherent melt layers are exceptionally bright in AR radargrams (e.g., Fig 3a).
283 The large dielectric contrast between the spatially coherent melt layer and the overlying, underlying, and
284 interior snow and firn layers results in high reflectivity at the interfaces. However, electromagnetic energy
285 still propagates downward through the high reflectivity layer into the deeper firn layers. Culberg et al., (2021)
286 recently demonstrated mapping the extent of spatially coherent melt layers formed following the 2012
287 melting season (Nghiem et al., 2012) via AR (Figs. 1c; 2).

288 **2.3   Empirical Algorithm**

289 **2.3.1 Temporal L-band Signatures over the Percolation Facies**

290 T^B expresses the satellite-observed magnitude of thermal emission and is influenced by the microwave
291 instrument's observation geometry as well as the depth- and time-integrated dielectric and geophysical
292 properties of the ice sheet (Ulaby et al., 2014). The most significant geophysical property influencing T^B is
293 the volumetric fraction of meltwater within the snow and firn pore space (Mätzler and Hüppi, 1989). During
294 the melting season, the upper snow and firn layers of the percolation facies are saturated with large
295 volumetric fractions of meltwater that percolates vertically into the deeper firn layers (Benson, 1960;

296 Humphrey et al., 2012). Increases in the volumetric fraction of meltwater results in rapid relative increases
297 in the imaginary part of the complex dielectric constant (Tiuiri et al., 1984). This typically increases T^B, and
298 decreases volume scattering and penetration depth. The L-band penetration depth can rapidly decrease
299 from tens to hundreds of meters to less than a meter, dependent on the local snow and firn conditions.
300 During the freezing season, surface and subsurface water-saturated snow and firn layers and embedded
301 ice structures subsequently refreeze. Decreases in the volumetric fraction of meltwater results in rapid
302 relative decreases in the imaginary part of the complex dielectric constant. This decreases T^B, and
303 increases volume scattering and penetration depth. The L-band penetration depth increases back to tens
304 to hundreds of meters on variable time scales.

305 We analyze melting and freezing seasons in temporal L-band signatures exhibited in T_V^B time series
306 over and near the AR- and MCoRDS-derived perennial firn aquifer and ice slab detections projected on the
307 NH EASE-Grid 2.0 (Fig. 4; Table 1). We project ice surface temperature observations calculated using
308 thermal infrared brightness temperature collected by the Moderate Resolution Imaging Spectroradiometer
309 (MODIS) on the Terra and Aqua satellites (Hall et al., 2012) on the NH EASE-Grid 2.0 at a 3.125 km rSIR
310 grid cell spacing. We then derive melt onset and surface freeze-up dates for each rSIR grid cell using the
311 methodology described in Miller et al., (2020). We set a threshold of ice surface temperature >−1°C for
312 meltwater detection (Nghiem et al., 2012), consistent with the ±1°C accuracy of the ice surface temperature
313 observations. For temperatures that are close to 0°C, ice surface temperatures are closely compatible with
314 contemporaneous NOAA near-surface air temperature observations (Shuman et al., 2014). Melt onset and
315 surface freeze-up dates are overlaid on T_V^B time series to partition the melting and freezing seasons. Melt
316 onset dates typically occur between April and July, and surface freeze-up dates typically occur between
317 July and September. The melting season increases in duration moving downslope from the dry snow facies,
318 and ranges from a single day in the highest elevations (>2500 m) of the percolation facies, to 150 days in
319 the ablation facies. Similarly, the freezing season decreases in duration moving downslope, and ranges
320 from between 215 days and 365 days.

321 Over perennial firn aquifer areas (e.g., Fig. 4a, SMAP Test Site A: 66.2115°N, 39.1795°W, 1625 m
322 a.s.l), maximum T_V^B ($T_{V,max}^B$) values are radiometrically warm during the melting season. Vertically
323 percolating meltwater and gravity-driven meltwater drainage seasonally recharges perennial firn aquifers
324 at depth (Fountain and Walder et al., 1998). Minimum T_V^B ($T_{V,min}^B$) values remain radiometrically warm during
325 the freezing season as a result of latent heat continuously released by the slow refreezing of the deeper
326 firn layers that are saturated with large volumetric fractions of meltwater (Miller et al, 2020). Temporal L-
327 band signatures exhibit slow exponential decreases and approach, and sometimes achieve, stable T_V^B
328 values. T_V^B can decrease by more than 50 K during the freezing season, which represents the descent of
329 the upper surface of stored meltwater by depths of meters to tens of meters beneath the ice sheet surface
330 (Miège et al., 2016).

331 Over ice slab areas (e.g., Fig. 4b, SMAP Test Site B: 66.8850°N, 42.7765°W, 1817 m a.s.l), $T_{V,max}^B$
332 values are typically radiometrically colder than over perennial firn aquifer areas during the melting season.

333 The presence of dense low-permeability solid-ice layers reduces the snow and firn pore space available to
334 store seasonal meltwater at depth. Meltwater may alternatively runoff ice slabs downslope towards the wet
335 snow facies. $T_{V,min}^B$ values are also typically radiometrically colder than over perennial firn aquifer areas
336 during the freezing season as a result of the absence of meltwater stored at depth. Temporal L-band
337 signatures exhibit exponential decreases that are slightly more rapid than over perennial firn aquifer areas,
338 and often achieve stable T_V^B values.

339 Over other percolation facies areas (e.g., Fig. 4c, SMAP Test Site C: 66.9024°N, 44.7528°W, 2350
340 m a.s.l), where seasonal meltwater is fully refrozen and stored exclusively as embedded ice, $T_{V,max}^B$ values
341 are typically radiometrically colder than over perennial firn aquifer and ice slab areas during the melting
342 season. $T_{V,min}^B$ values are also typically radiometrically cold during the freezing season. Temporal L-band
343 signatures exhibit rapid exponential decreases, and achieve stable T_V^B values. However, over the highest
344 elevations (>2500 m a.s.l.) of the percolation facies approaching the dry snow line, where seasonal surface
345 melting and the formation of embedded ice structures is limited, $T_{V,min}^B$ values remain radiometrically warm
346 during the freezing season. T_V^B decreases, often step-responses exceeding 10 K, are a result of an increase
347 in volume scattering from newly formed embedded ice structures within a spatially coherent melt layer.
348 Temporal L-band signatures that increase several K on time scales of years indicate the burial of spatially
349 coherent melt layers formed following the 2010, 2012, 2015, and 2018 melting seasons by snow
350 accumulation.

351 Exponentially decreasing temporal L-band signatures transition smoothly between perennial firn
352 aquifer, ice slab, and other percolation facies areas – there are no distinct temporal L-band signatures that
353 delineate boundaries between these sub-facies. Boundary transitions between the dry snow facies and the
354 wet snow facies, however, are delineated above and below the percolation facies. Over the dry snow facies
355 (e.g., Fig. 4d, SMAP Test Site D: 66.3649°N, 43.2115°W, 2497 m a.s.l), $T_{V,max}^B$ and $T_{V,min}^B$ values are
356 radiometrically warm during the melting and freezing seasons. Temporal L-band signatures that increase
357 on time scales of years are observed throughout the dry snow facies at elevations as high as Summit
358 Station (3200 m a.s.l) and indicate the burial of the spatially coherent melt layer formed following the 2012
359 melting season (Nghiem et al., 2012) by snow accumulation (Culberg et al., 2021). Over the wet snow
360 facies (e.g., Fig. 4e, SMAP Test Site E: 67.3454°N, 48.4789°W, 1469 m a.s.l), where seasonal meltwater
361 is fully refrozen and stored as superimposed ice, $T_{V,max}^B$ values are radiometrically warm during the melting
362 season. As compared to the percolation facies, where temporal L-band signatures exhibit rapid increases
363 following melt onset, temporal L-band signatures reverse and exhibit rapid decreases. These reversals are
364 a result of high reflectivity and attenuation at the fully water-saturated snow layer and/or at the wet rough
365 superimposed ice-air interface. Meltwater runs-off superimposed ice downslope towards the ablation facies.
366 $T_{V,min}^B$ values remain radiometrically warm during the freezing season. Temporal L-band signatures exhibit
367 rapid increases, and achieve stable T_V^B values.

368 ### 2.3.2 Two-Layer-L-band Brightness Temperature Model

369   Based on our analysis of $T^B_{V,max}$ and $T^B_{V,min}$ in temporal L-band signatures over the percolation facies

370   (Section 2.3.1), we derive a 'firn saturation' parameter using a simple two-layer L-band brightness

371   temperature model (Ashcraft and Long, 2006). The 'firn saturation' parameter is similar to the 'melt intensity'

372   parameter derived in Hicks and Long (2011) that uses enhanced resolution vertically-polarized Ku-band

373   radar backscatter imagery (2003) collected by the SeaWinds radar scatterometer that was flown in tandem

374   on NASA's Quick SCATterometer (QuikSCAT) satellite (Tsai et al., 2000) and JAXA's Advanced Earth

375   Observing Satellite 2 (ADEOS-II) (Freilich et al., 1994). We use the firn saturation parameter to estimate

376   the maximum seasonal volumetric fraction of meltwater within the saturated upper snow and firn layers of

377   the percolation facies using $T^B_{V,max}$ and $T^B_{V,min}$ values extracted from T^B_V time series. We calculate the firn

378   saturation parameter for each rSIR grid cell within the ice -masked extent of the GrIS as part of our adapted

379   empirical algorithm (Section 2.3.4).

380   We assume a base layer underlying a water-saturated firn layer with a given depth and volumetric

381   fraction of meltwater. Each of the layers is homogenous. The ice sheet is discretely layered to calculate T^B_V

382   at an oblique incidence angle (Eq. 1). Emission from the base layer is a function of both the macroscopic

383   roughness and the dielectric properties of the layer. It occurs in conjunction with volume scattering at depth,

384   and is locally dependent on embedded ice structures, spatially coherent melt layers, ice slabs, and

385   perennial firn aquifers. Reflectivity at depth (i.e., at the base layer-water-saturated firn layer interface), and

386   at the ice sheet surface (i.e., at the water-saturated firn layer-air interface) is neglected. The contribution

387   from each layer is individually calculated.

388   The two-layer L-band brightness temperature model is represented analytically by

389    $$T^B_{V,max} = T\left(1 - e^{-\kappa_e d sec\theta}\right) + T^B_{V,min}e^{-\kappa_e d sec\theta} \ , \tag{Eq. 1}$$

390   where $T^B_{V,max}$ is the maximum vertically-polarized L-band brightness temperature at the ice sheet surface,

391   and represents emission from the maximum seasonal volumetric fraction of meltwater stored within the

392   water-saturated firn layer. $T^B_{V,min}$ is the minimum vertically-polarized L-band brightness temperature

393   emitted from the base layer. T is the physical temperature of the water-saturated firn layer, θ is the

394   transmission angle, κ_e is the extinction coefficient, and d is depth.

395   We invert Eq. 1 and solve for the firn saturation parameter (ξ)

396    $$\xi = ln\left(\frac{T^B_{V,max}-T}{T^B_{V,min}-T}\right)cos\theta \ , \tag{Eq. 2}$$

397   where $\xi = \kappa_e d$. The maximum vertically-polarized L-band brightness temperature asymptotically approaches

398   the physical temperature of the water-saturated firn layer as the extinction coefficient and the depth of the

399   water-saturated firn layer increases. For simplicity, we follow Jezek et al., (2015) and define the extinction

400   coefficient as the sum of the Raleigh scattering coefficient (κ_s) and the absorption coefficient (κ_a). This

401   assumes scattering from snow grains, which are small (millimeter scale) relative to the L-band wavelength

402   (21 cm), and neglects Mie scattering from large (centimeter scale) embedded ice structures. However, for

403   water-saturated firn, absorption dominates over scattering, and increases in the extinction coefficient are
404   controlled by the volumetric fraction of meltwater (m_v).

405   We assume that thicker water-saturated firn layers with larger volumetric fractions of meltwater
406   generate higher firn saturation parameter values. However, the thickness of the water-saturated firn layer
407   is limited by the L-band penetration depth. Theoretical L-band penetration depths calculated for a water-
408   saturated firn layer range from between 10 m for small volumetric fractions of meltwater (m_v<1%), and 1
409   cm for large volumetric fractions of meltwater (m_v=20%) (Fig. 5). Large volumetric fractions of meltwater
410   results in high reflectivity and attenuation at the water-saturated firn layer-air interface, and a radiometrically
411   cold firn layer.

2.3.3 Continuous Logistic Model

413   We adapt our previously developed empirical algorithm to map the extent of Greenland's perennial firn
414   aquifers (Miller et al., 2020) to also map the extent of ice slab areas. The empirical algorithm is derived from
415   the continuous logistic model, which is based on a differential equation that models the decrease in physical
416   systems as a function of time using a set of sigmoidal curves. These curves begin at a maximum value with
417   an initial interval of decrease that is approximately exponential. Then, as the function approaches its
418   minimum value, the decrease slows to approximately linear. Finally, as the function asymptotically reaches
419   its minimum value, the decrease exponentially tails off and achieves stable values. We use the continuous
420   logistic model to parametrize the refreezing rate within the water-saturated upper snow and firn layers of
421   the percolation facies using T_V^B time series that are partitioned using $T_{V,max}^B$ and $T_{V,min}^B$ values. We calculate
422   the refreezing rate for each rSIR grid cell within the percolation facies extent as part of our adapted empirical
423   algorithm (Section 2.3.4).

424   The continuous logistic model is described by a differential equation known as the logistic equation

425    $$\frac{dx}{dt} = \zeta x (1 - x) \hspace{6cm} \text{(Eq. 3)}$$

426   that has the solution

427    $$x(t) = \frac{1}{1 + \left(\frac{1}{x_o} - 1\right) e^{-\zeta t}} , \hspace{5cm} \text{(Eq. 4)}$$

428   where x_o is the function's initial value, ζ is the function's exponential rate of decrease, and t is time. The
429   function $x(t)$ is also known as the sigmoid function. We use the sigmoid function to model the exponentially
430   decreasing temporal L-band signatures observed over the percolation facies as a set of decreasing
431   sigmoidal curves.

432   We first normalize T_V^B time series for each rSIR grid cell

433    $$T_{V,N}^B(t) = \frac{T_V^B(t) - T_{V,min}^B}{T_{V,max}^B - T_{V,min}^B} , \hspace{4.5cm} \text{(Eq. 5)}$$

434   where $T_{V,min}^B$ is the minimum vertically-polarized L-band brightness temperature, and $T_{V,max}^B$ is the maximum
435   vertically-polarized L-band brightness temperature. We then apply the sigmoid fit

436 $$T_{V,N}^B\big(t \in [t_{max}, t_{min}]\big) = \cfrac{1}{1+\left(\cfrac{1}{T_{V,N}^B(t_{max})}-1\right)e^{-\zeta t}} .$$ (Eq. 6)

437 $T_{V,N}^B\big(t \in [t_{max}, t_{min}]\big)$ is the normalized vertically-polarized L-band brightness temperature on the time

438 interval $t \in [t_{max}, t_{min}]$, where t_{max} is the time the function achieves a maximum value, and t_{min} is the

439 time the function achieves a minimum value. The initial normalized vertically-polarized L-band brightness

440 temperature ($T_{V,N}^B(t_{max})$) is the function's maximum value. The final normalized vertically-polarized L-band

441 brightness temperature ($T_{V,N}^B(t_{min})$) is the function's minimum value. The function's exponential rate of

442 decrease represents the refreezing rate parameter (ζ). An example set of simulated sigmoidal curves is

443 shown in Fig. 6.

2.3.4 SMAP-Derived Perennial Firn Aquifer and Ice Slab Mapping

445 Our adapted empirical algorithm is implemented in two steps: (1) mapping the extent of the percolation

446 facies using the firn saturation parameter derived from the simple two-layer L-band brightness temperature

447 model (Section 2.3.2), and (2) mapping the extent of perennial firn aquifer and ice slab areas over the

448 percolation facies using the continuous logistic model (Section 2.3.3) we calibrate using airborne ice-

449 penetrating radar surveys (Section 2.2).

450 Using Eq. 2, we first set a threshold for the firn saturation parameter (ξ_T) defined by the relationship

451 $$\xi_T = (\kappa_s + \kappa_a)d \leq \xi .$$ (Eq. 7)

452 We calculate the Raleigh scattering coefficient (κ_s) in Eq. 7 using

453 $$\kappa_s = N_d \frac{8}{3}k_o^4 r^6 \left|\frac{\varepsilon_r-1}{\varepsilon_r+2}\right|^2 ,$$ (Eq. 8)

454 where N_d is the particle density, k_o is the wave number of the background medium of air, r is the snow

455 grain radius set to r=2 mm, and ε_r is the complex dielectric constant. The particle density is defined by

456 $$N_d = \frac{\rho_{firn}}{\rho_{ice}}\frac{1}{\frac{4}{3}\pi r^3} ,$$ (Eq. 9)

457 where ρ_{firn} is firn density set to ρ_{firn}=400 kg/m³, and ρ_{ice} is ice density set to ρ_{ice}=917 kg/m³. Our grain

458 radius and firn density estimates are consistent with measurements within the upper snow and firn layers

459 of the percolation facies of south eastern Greenland at the Helheim Glacier field site (Fig. 2a, blue circle),

460 where in situ perennial firn aquifer measurements have recently been collected (Miller et al., 2017).

461 We calculate the absorption coefficient (κ_a) in Eq. 7 using

462 $$\kappa_a = -2k_o \Im\{\sqrt{\varepsilon_r}\} ,$$ (Eq. 10)

463 where $\Im\{\}$ represents the imaginary part. We calculate the complex dielectric constant of the water-

464 saturated firn layer in Eq. 8 and Eq. 10 using the empirically derived models described in Tiuri et al., (1984).

465 We set the volumetric fraction of meltwater to m_v=1%. We set the depth of the water-saturated firn layer in

466 Eq. 7 to d=1 m. These values are consistent with typical lower frequency (e.g., 37 GHz, 13.4 GHz, 19 GHz)

467 passive (e.g., Mote, et al. 1995; Abdalati and Steffen, 1997; Ashcraft and Long, 2006) and active (e.g.,

468   Hicks and Long, 2011) microwave algorithms used to detect seasonal surface melting over the GrIS. Using

469   the results of Eq. 7, 8, 9, and 10, we calculate the firn saturation parameter threshold to be ξ_T=0.1.

470   The first step in our adapted empirical algorithm is to map the extent of the percolation facies. For

471   each rSIR grid cell within the ice -masked extent of the GrIS, we smooth the corresponding T_V^B time series

472   using a 14-observation (1 week) moving window. We extract the minimum vertically-polarized L-band

473   brightness temperature ($T_{V,min}^B$), and the maximum vertically-polarized L-band brightness temperature

474   ($T_{V,max}^B$). We set the physical temperature of the water-saturated firn layer to T=273.15 K, and the

475   transmission angle to θ=40°. We then calculate the firn saturation parameter (ξ) using Eq. 2. If the

476   calculated firn saturation parameter exceeds the firn saturation parameter threshold, the rSIR grid cell is

477   converted to a binary parameter to map the total extent of the percolation facies.

478   We note that smoothing T_V^B time series will mask brief low-intensity seasonal surface melting that

479   occurs in the high-elevation (>2500 m) percolation facies, where seasonal meltwater is rapidly refrozen

480   within the colder snow and firn layers (e.g., Fig. 4d). Thus, the calculated firn saturated parameter will not

481   exceed the firn saturation parameter threshold, and these rSIR grid cells are excluded from the algorithm.

482   The exclusion of rSIR grid cells in the high-elevation percolation facies is not expected to have a significant

483   impact on our results as our algorithm targets rSIR grid cells in areas that experience intense seasonal

484   surface melting. The exclusion of rSIR grid cells may slightly underestimate the mapped percolation facies

485   extent.

486   The second step in our adapted empirical algorithm is to map the extent of perennial firn aquifer

487   and ice slab areas over the percolation facies. For each rSIR grid cell within the mapped percolation facies

488   extent, we normalize the corresponding T_V^B time series ($T_{V,N}^B(t)$) using Eq. 5. We then extract the initial

489   normalized vertically-polarized L-band brightness temperature ($T_{V,N}^B(t_{max})$) and the final normalized

490   vertically-polarized L-band brightness temperature ($T_{V,N}^B(t_{min})$), and partition $T_{V,N}^B(t)$ on the time interval $t \in$

491    $[t_{max}, t_{min}]$. We smooth $T_{V,N}^B(t \in [t_{max}, t_{min}])$ using a 56-observation (4 week) moving window. The

492   sigmoid fit is then iteratively applied using Eq. 6. Smoothing reduces the chi-squared error statistic when

493   fitting $T_{V,N}^B(t \in [t_{max}, t_{min}])$ to the sigmoid function. We fix the initial normalized vertically-polarized L-band

494   brightness temperature at $T_{V,N}^B(t_{max})$=0.99, which provides a uniform parameter space in which the

495   refreezing rate parameter (ζ) can be analyzed. Variability in $T_{V,N}^B(t_{max})$ is controlled by the volumetric

496   fraction of meltwater within the upper snow and firn layers of the percolation facies, and is accounted for in

497   the firn saturation parameter (ξ), which is analyzed separately. $T_{V,N}^B(t \in [t_{max}, t_{min}])$ iteratively fit to the

498   sigmoid function converge quickly (i.e., algorithm iterations I ∈ [5, 15]), and observations are a good fit (i.e.,

499   chi squared error statistic is $\chi 2 \in [0, 0.1]$).

500   Using the SMAP-derived $T_{V,N}^B(t_{max})$ and $T_{V,N}^B(t_{min})$, rather than the MODIS-derived initial

501   normalized vertically-polarized L-band brightness temperature at the surface freeze-up date ($T_{V,N}^B(t_{sfu})$),

502   and final normalized vertically-polarized L-band brightness temperature at the melt onset date ($T_{V,N}^B(t_{mo})$)

503   that were used in the empirical algorithm described in Miller et al., 2020 has several advantages. They key

504 advantage of this approach is that maps can be generated using T^B imagery collected from a single satellite,

505 which simplifies our adapted empirical algorithm. Another advantage is that unlike T^B collected at shorter-

506 wavelength thermal infrared frequencies (e.g., MODIS), T^B collected at longer wavelength microwave

507 frequencies (e.g., SMAP) is not sensitive to clouds, which eliminates observational gaps and cloud

508 contamination, and provides more accurate time series partitioning and more robust curve fitting.

509 We calibrate our adapted empirical algorithm using the AR- and MCoRDS-derived perennial firn

510 aquifer and ice slab detections projected on the NH EASE-Grid 2.0. For each rSIR grid cell with at least

511 one detection, we extract the correlated maximum vertically-polarized L-band brightness temperature

512 ($T^B_{V,max}$), the minimum vertically-polarized L-band brightness temperature ($T^B_{V,min}$), the firn saturation

513 parameter (ξ), and the refreezing rate parameter (ζ). For each of the extracted calibration parameters, we

514 calculate the standard deviation (σ). Thresholds of $\pm 2\sigma$ are set in an attempt to eliminate peripheral rSIR

515 grid cells near the ice sheet edge and near the boundaries of each sub-facie, where L-band emission can

516 be influenced by morphological features, such as crevasses, superimposed and glacial ice, and spatially

517 integrated with emission from rock, land, the ocean, and adjacent percolation facies and wet snow facies

518 areas. The calibration parameter intervals are given in Table 2**.** We apply the calibration to each rSIR grid

519 cell within the percolation facies extent. If the extracted calibration parameters are within the intervals, the

520 rSIR grid cell is converted to a binary parameter to map the total extent of each of these sub-facies.

521 Miller et al., 2020 cited significant uncertainty in the SMAP-derived perennial firn aquifer extent as

522 a result of the lack of a distinct temporal L-band signature delineating the boundary between perennial firn

523 aquifer areas and adjacent percolation facies areas. In this study, similar uncertainty exists in the SMAP-

524 derived perennial firn aquifer and ice slab extents. This uncertainty could, at least in part, be a result of the

525 rSIR algorithm. An rSIR grid cell corresponds to the weighted average of T^B over SMAP's antenna footprint

526 (Long et al., 2020). The weighting is the grid cell's spatial response function (SRF), which is approximately

527 18 km (i.e., the effective resolution) in diameter. The SRF is centered on the rSIR grid cell. Since the

528 effective resolution (i.e., the size of the 3 dB contour of the SRF) is less than the rSIR grid cell spacing,

529 rSIR grid cell SRF's overlap and the grid cells T^B values are not statistically independent. This uncertainty,

530 however, could also have a geophysical basis, as it is unlikely that the boundaries between sub-facies as

531 well as between facies are distinct. The thickness of the water-saturated firn layer or ice slab may thin and

532 taper-off at the periphery, and sub-facies and facies may become spatially scattered and merge together.

533 The limited extent (AR, 15 m x 20 m; MCoRDS, 14 m x 40 m) of the airborne ice-penetrating radar

534 surveys as compared to the rSIR grid cell extent (3.125 km) and the effective resolution of the SMAP

535 enhanced-resolution T^B_V imagery is also cited in Miller et al., 2020 as a source of uncertainty in the empirical

536 algorithm. In this study, similar uncertainty exists in our adapted empirical algorithm. The total rSIR grid cell

537 extent with airborne ice-penetrating radar survey coverage is less than 2%. Thus, 98% of the total rSIR grid

538 cell extent from which the SMAP-derived calibration parameter intervals are extracted is unknown.

539 Calculating the total rSIR grid cell extent where detections are absent along OIB flight lines and statistically

540 integrating this calculation into the multi-year calibration technique may help reduce the uncertainty,

541 particularly the significant uncertainty in the interannual variability in extent, which we have yet to resolve.

542 A sensitivity analysis suggests that even small changes in the SMAP-derived calibration parameter intervals

543 (i.e., several K for $T^B_{V,min}$, and $T^B_{V,max}$, several tenths of a percentage point for ξ, and several hundredths of

544 a percentage point for ζ) can result in variability in the mapped extents of hundreds of square kilometers,

545 and boundary transitions between perennial firn aquifer and ice slab areas. Thus, the mapped extent of

546 each of these sub-facies should simply be considered an initial result demonstrating the potential of our

547 adapted empirical algorithm for future work.

3.   Results and Discussion

549 The SMAP-derived maximum vertically-polarized L-band brightness temperature values generated by our

550 adapted empirical algorithm range from between $T^B_{V,max}$=150 K and 275 K, and the minimum vertically-

551 polarized L-band brightness temperature values range from between $T^B_{V,min}$=130 K and 250 K. These values

552 are consistent with the range of $T^B_{V,max}$ and $T^B_{V,min}$ values given in the temporal L-band signature analysis

553 (Table 1). Firn saturation parameter values range from between ξ=0.1 and 4.0. Refreezing rate parameter

554 values range from between ζ=-0.09 and -0.01. The observed lower bound (ζ=-0.09) of the refreezing rate

555 parameter is significantly higher than the predicted lower bound (ζ=-1) in our example set of simulated

556 sigmoidal curves (black line, Fig. 6).

557   The SMAP-derived perennial firn aquifer, ice slab, and percolation facies extents are shown in Figs.

558 7a-9a. The percolation facies extent (5.8 x 10^5 km^2) is mapped at elevations between 500 m a.s.l. and

559 3000 m a.s.l., and extends over 32 % of the GrIS extent (1.8 x 10^6 km^2). The perennial firn aquifer extent

560 (64,000 km^2) is mapped at elevations between 600 m a.s.l and 2600 m a.s.l., and extends over 11% of the

561 percolation facies extent, and 4% of the GrIS extent. Predominately high $T^B_{V,max}$, $T^B_{V,min}$, ξ, and ζ values

562 mapped within the perennial firn aquifer extent indicates the widespread presence of thicker water-

563 saturated firn layers with larger volumetric fractions of meltwater that are radiometrically warm during both

564 the melting and freezing seasons, and have extended refreezing rates. The ice slab extent (76,000 km^2) is

565 mapped at elevations between 800 m a.s.l and 2700 m a.s.l., and extends over 13 % of the percolation

566 facies extent, and 4 % of the GrIS extent. As compared to perennial firn aquifer areas, decreased $T^B_{V,max}$,

567 $T^B_{V,min}$, ξ and ζ values in ice slabs areas indicates the presence of thinner water-saturated firn layers with

568 lower volumetric fractions of meltwater that are radiometrically colder, and have slightly more rapid

569 refreezing rates. Combined together, the total extent (140,000 km^2) is the equivalent of 24% of the

570 percolation facies extent, and 10% of the GrIS extent. The extents of these sub-facies are generally isolated

571 and somewhat scattered within the percolation facies. However, in several areas in south, south and central

572 eastern, and northern Greenland, the sequential formation of facies and sub-facies (dry snow facies -

573 percolation facies - ice slab - perennial firn aquifer – ablation facies) are mapped.

574   Figs. 7b-9b shows perennial firn aquifers, ice slabs, and spatially coherent melt layers detected by

575 airborne ice-penetrating radar surveys overlaid on the SMAP-derived percolation facies extent. The SMAP-

576   derived perennial firn aquifer extent mapped in southern, and south and central eastern Greenland is
577   consistent with the AR- and MCoRDS-derived perennial firn aquifer detections. Additional smaller perennial
578   firn aquifer areas are mapped in northern Greenland. The SMAP-derived ice slab extent mapped in south
579   western, and central eastern Greenland is generally consistent with the spatial patterns of the AR-derived
580   ice slab detections, however, is significantly expanded upslope in each of these areas. In northern
581   Greenland, perennial firn aquifers areas are alternatively mapped, and additional expansive ice slab areas
582   are mapped upslope of perennial firn aquifer areas. Additional smaller ice slab areas are mapped in south
583   and south eastern Greenland. We note that the AR- and MCoRDS-derived perennial firn aquifer and ice
584   slab detections are limited in space and time, particularly in northern Greenland, with a time interval as
585   large as nine years between the airborne ice-penetrating radar surveys and the SMAP enhanced-resolution
586   T_V^B imagery we use in our adapted empirical algorithm. In western and northern Greenland, the 2015 melting
587   season was especially intense (Tedesco et al., 2016). And, in northern Greenland, the ablation facies have
588   recently (2010-2019) increased in extent (Noël et al., 2019), and supraglacial lakes have recently (2014-
589   2019) advanced inland (Turton et al., 2021), indicating a possible geophysical basis for the observed
590   formation, boundary transitions, and expansion. Neither perennial firn aquifer or ice slab areas are mapped
591   on the Maniitsoq and Flade Isblink Ice Caps, where spatially integrated L-band emission results in
592   calibration parameter values outside the defined intervals for each of these sub-facies.

593   Although the AR-derived spatially coherent melt layers detections are often observed to be adjacent
594   to perennial firn aquifer and ice slab areas, these sub-facies were masked in the original airborne ice
595   penetrating radar survey analysis by Culberg et al., (2021). Spatially coherent melt layers often overlay
596   perennial firn aquifers (e.g., Fig. 3a), and merge with ice slabs (Culberg et al., 2021; Fig.4).

597   Shallow buried supraglacial lakes have recently been identified within the percolation facies of
598   western, northern, and north and central eastern Greenland using airborne ice-penetrating radar surveys
599   (Koenig et al., 2015) and satellite synthetic aperture radar imagery (Miles et al., 2017; Schröder et al., 2020;
600   Dunmire et al., 2021). These buried supraglacial lakes are within the SMAP-derived perennial firn aquifer
601   and ice slab extents, however, are not expected to significantly influence L-band emission in these areas
602   for two reasons. (1) As compared to SMAP's 18 km footprint, the mean extent of buried supraglacial lakes
603   is limited (less than 1 km^2), and they are sparsely distributed in perennial firn aquifer and ice slab areas
604   (Dunmire et al., 2021). (2) Supraglacial lakes form during the melting season as a result of meltwater
605   storage within topographic depressions at the ice sheet surface (Echelmeyer et al. 1991). Similar to
606   subglacial lakes (Jezek et al., 2015) and perennial firn aquifers (Miller et al., 2020), supraglacial lakes
607   represent radiometrically cold near-surface meltwater reservoirs. Upwelling L-band emission from deeper
608   firn layers, superimposed and/or glacial ice, and the underlying bedrock are effectively blocked by high
609   reflectivity and attenuation at the interface between the lake bottom and the underlying impermeable layer.
610   This results in low observed T^B at the upper surface of meltwater stored within supraglacial lakes. During
611   the freezing season, the upper surface of meltwater refreezes and forms a partial or solid-ice cap that is
612   sometimes buried by snow accumulation (Koenig et al., 2015). Airborne ice-penetrating radar surveys in

613 April and May between 2009 and 2012 suggest the mean depth to the upper surface of meltwater stored
614 within buried supraglacial lakes is approximately 2 m (Koenig et al., 2015). Over buried supraglacial lakes,
615 L-band emission from the refreezing partial or solid-ice cap, which is smooth relative to the L-band
616 wavelength (21 cm), likely induces surface scattering. As a result, T_V^B decreases over buried supraglacial
617 lakes are likely negligible. Thus, over SMAP's 18 km footprint, we postulate water-saturated firn layers
618 dominate L-band emission over the percolation facies of the GrIS.

619 The SMAP-derived perennial firn aquifer extent (64,000 km[2]) generated by our adapted empirical
620 algorithm and the multi-year calibration technique (2015-2019) is consistent with the extent (66,000 km[2])
621 generated by the previously developed empirical algorithm and the single-coincident year calibration
622 technique (2016) described in Miller et al., 2020. The SMAP-derived perennial firn aquifer extent is generally
623 consistent with previous C-band (5.3 GHz) satellite radar scatterometer-derived perennial firn aquifer
624 extents mapped using the Advanced SCATterometer (ASCAT) on the European Organization for the
625 Exploitation of Meteorological Satellites (EUMETSAT) Meteorological Operational A (MetOp-A) satellite
626 (2009-2016, 52 000-153 000 km[2]; Miller, 2019), and the Active Microwave Instrument in radar scatterometer
627 mode (ESCAT) on ESA's European Remote Sensing (ERS) satellite series (1992-2001, 37 000-64 000 km[2];
628 Miller, 2019) as well as the C-band (5.4 GHz) synthetic aperture radar-derived extent mapped using ESA's
629 Sentinel-1 satellite (2014-2019, 54 000 km[2]; Brangers et al., 2020). The exception is the ASCAT-derived
630 perennial firn aquifer extent (2012-2013, 153,000 km[2]; Miller, 2019) mapped following the 2012 melting
631 season (Nghiem et al., 2012) in which significant changes in the dielectric and geophysical properties that
632 influence radar backscatter likely occurred. The unreasonably expansive (i.e., more than twice the mean)
633 mapped extent is a result of ASCAT'S shallow (several meters) C-band penetration depth (Jezek et al.,
634 1994), and the simple threshold-based algorithm, which was not calibrated for an extreme melting season
635 that included saturation of the upper snow and firn layers of the dry snow facies and percolation facies with
636 relatively large volumetric fractions of meltwater (Miller et al., 2019). Water-saturated firn layers had
637 extended refreezing rates, however, seasonal meltwater was not stored at depth. Widespread spatially
638 coherent melt layers were alternatively formed in many of the mapped areas (Culberg et al., 2021). The
639 SMAP-derived ice slab extent (76,000 km[2]) is also consistent with previous AR-derived ice slab extents
640 (2010-2014, 64,800 km[2]-69,400 km[2]; MacFerrin et al., 2019).

641 Although we simply consider our mapped extents a high-probability area for preferential formation,
642 the maps generated by our adapted empirical algorithm and the multi-year calibration technique for
643 individual years suggest there reasonable interannual variability in perennial firn aquifer and ice and slab
644 extents (Table 3). Our results demonstrate sensitivity to the variability in the depth- and time-integrated
645 dielectric and geophysical properties of the percolation facies that influence the radiometric temperature,
646 even during the 2015 melting season (Tedesco et al., 2016).

4 Implications

648 Seasonal surface melting over the GrIS has increased in extent, intensity, and duration since early in the
649 satellite era (Steffen et al., 2004; Tedesco e al., 2008; Tedesco et al., 2011; Nghiem et al., 2012; Tedesco

650 et al., 2016; Tedesco and Fettweis, 2020; Cullather et al., 2020). Consistent with recent seasonal surface
651 melting trends, meltwater runoff has accelerated to become the dominant mass loss mechanism over the
652 GrIS (van den Broeke et al., 2016). Meltwater storage in both solid (i.e., embedded ice structures, including
653 ice slabs, and spatially coherent melt layers) and liquid (i.e., perennial firn aquifers) form can buffer
654 meltwater runoff in the percolation facies and delay its eventual release into the ocean (Harper et al., 2012).
655 However, significant uncertainty remains in meltwater runoff estimates as a result of the lack of knowledge
656 of heterogeneous infiltration and refreezing processes within the snow and firn layers (Pfeffer and
657 Humphrey, 1996), and the depths to which meltwater can descend beneath the ice sheet surface
658 (Humphrey et al., 2012).

659   If the increasing seasonal surface melting trend continues (Franco et al., 2013; Noël et al., 2021),
660 perennial firn aquifer formation and expansion may increase the possibility of crevasse-deepening via
661 meltwater-induced hydrofracturing (Alley et al., 2005; van der Veen, 2007), especially if crevasse fields
662 expand into perennial firn aquifer areas as a result of accelerated ice flow (Colgan et al., 2016). Meltwater-
663 induced hydrofracturing is an important component of supraglacial lake drainage during the melting season
664 (Das et al., 2008; Stevens et al., 2015) leading to at least temporary localized accelerated ice flow velocities
665 (Zwally et al., 2002; Joughin et al., 2013; Moon et al., 2014) as well as ice discharge from outlet glaciers
666 (Chudley et al., 2019), and mass balance changes (Joughin et al., 2008). Perennial firn aquifers may also
667 support meltwater-induced hydrofracturing, even during the freezing season (Poinar et al., 2017; Poinar et
668 al., 2019).

669   The formation and expansion of ice slabs reduces permeability within the upper snow and firn
670 layers and facilitates lateral meltwater flow with minimum vertical percolation into the deeper firn layers,
671 thereby enhancing meltwater runoff and mass loss at the periphery (Machguth et al., 2016; MacFerrin et
672 al., 2019). Lateral meltwater flow across ice layers overlying deeper permeable firn layers was first
673 postulated by Müller (1962). The theory was then further developed by Pfeffer et al., (1991) as an end-
674 member case for meltwater runoff in the percolation facies, with the other end member case being lateral
675 meltwater flow across superimposed ice. Lateral meltwater flow and high-elevation (1850 m a.s.l) meltwater
676 runoff across ice slabs in the percolation facies was first observed in visible satellite imagery collected by
677 the NASA-USGS Landsat 7 mission during the 2012 melting season (Machguth et al., 2016).

678   Spatially coherent melt layers represent a recently identified refreezing mechanism in the dry snow
679 facies (Nghiem et al., 2002; Culberg et al., 2021). Similar to ice slabs, the formation and expansion of
680 spatially coherent melt layers reduces the pore space within the upper snow and firn layers, and can limit
681 meltwater flow with minimum vertical percolation into the deeper firn layers, thereby potentially
682 preconditioning the dry snow facies for the formation of ice slabs and enhanced meltwater runoff from
683 significantly higher elevations on accelerated time scales. If spatially coherent melt layers merge with ice
684 slabs upslope of perennial firn aquifers areas they might also simultaneously accelerate both meltwater
685 runoff and meltwater-induced hydrofracturing during extreme melting seasons. The formation of spatially
686 coherent melt layers overlying deeper perennial firn aquifers may result in the formation of shallow perched

687 firn aquifers (Culberg et al., 2021), or may terminate gravity-driven meltwater drainage and seasonal

688 recharging (Fountain and Walder, 1998), which may eventually completely refreeze stored meltwater into

689 ice slabs or decameters thick solid-ice layers overlying deeper glacial ice.

5   Summary and Future Work

691 In this study, for the first time, we have demonstrated the novel use of the L-band microwave radiometer

692 on NASA's SMAP satellite for mapping perennial firn aquifers and ice slabs together as a continuous system

693 over the percolation facies of the GrIS. We have adapted our previously developed empirical algorithm

694 (Miller et al., 2020) by expanding our analysis of spatiotemporal differences in SMAP enhanced-resolution

695 T_V^B imagery and temporal L-band signatures. We have used this analysis to derive a firn saturation

696 parameter from a simple two-layer L-band brightness temperature model . And, we have used the firn

697 saturation parameter to map the extent of the percolation facies. We have found that by correlating

698 maximum and minimum T_V^B values, the firn saturation parameter, and the refreezing rate parameter with

699 perennial firn aquifer and ice slab detections identified via the CReSIS AR and MCoRDS instruments flown

700 by NASA's OIB campaigns that we can calibrate our previously developed empirical algorithm (Miller et al.,

701 2020) to map plausible extents.

702   We note that significant uncertainty exists in the mapped extents as a result of: (1) correlating the

703 SMAP-derived parameters with airborne ice-penetrating radar detections that are not coincident in time, (2)

704 the lack of a distinct temporal L-band signature delineating the boundary between perennial firn aquifer

705 areas, ice slabs areas, and adjacent percolation facies areas, and (3) the limited extent of the airborne ice-

706 penetrating radar detections as compared to the rSIR grid cell extent and the effective resolution of the

707 SMAP enhanced-resolution T_V^B imagery.

708   Miller et al., (2020) normalized SMAP enhanced-resolution T_V^B time series and converted the

709 exponential rate of T_V^B decrease over perennial firn aquifer areas to a binary parameter to map extent. In

710 this study, we have converted the SMAP-derived parameters to binary parameters to map the extent of

711 both perennial firn aquifer and ice slab areas. Moreover, we have included additional analysis of the

712 spatiotemporal differences in maximum and minimum T_V^B values, the firn saturation parameter, and the

713 refreezing rate parameter. We have shown that spatiotemporal differences in the SMAP-derived

714 parameters are consistent with our assumption of spatiotemporal differences in the englacial hydrology and

715 thermal characteristics of firn layers at depth.

716   Future work will focus on simulating temporal L-band signatures observed over perennial firn

717 aquifer and ice slab areas for a wide range of geophysical properties. Additionally, we will simulate the

718 distinct temporal L-band signatures observed over spatially coherent melt layers and explore mapping the

719 extent. Combining multi-layer depth-integrated L-band brightness temperature models (e.g., Jezek et al.,

720 2015) that include embedded ice structure parametrizations (e.g., Jezek et al., 2018) with models of depth-

721 dependent geophysical parameters can lead to an improved understanding of the extremely complex and

722 poorly described physics controlling L-band emission over the percolation facies. The development of more

723 sophisticated empirical algorithms that incorporate multi-layer depth-integrated L-band brightness
724 temperature models that are constrained by in situ measurements can help reduce the significant
725 uncertainty in the current mapped extents, and provide more accurate boundary delineation that can be
726 used to further quantify the interannual variability in future mapped extents of perennial firn aquifer, ice slab
727 and spatially coherent melt layer areas.

Data Availability

729 SMAP Radiometer Twice-Daily rSIR-Enhanced EASE-Grid 2.0 Brightness Temperatures, Version 1 (2015-
730 2019) have been produced as part of the NASA Science Utilization of SMAP project and are available at
731 https://doi.org/10.5067/QZ3WJNOUZLFK (Brodzik et al., 2019). The NASA MEaSUREs Greenland Ice
732 Mapping Project (GIMP) Land Ice and Ocean Classification Mask, Version 1, is available at
733 https://doi.org/10.5067/B8X58MQBFUPA (Howat, 2017), and the Digital Elevation Model, Version 1, is
734 available at https://nsidc.org/data/nsidc-0645/versions/1 (Howat et al., 2015). The coastline data are
735 available from GSHHG – A Global Self-consistent, Hierarchical, High-resolution Geography Database
736 https://doi.org/10.1029/96JB00104 (Wessel and Smith, 1996). Ice surface temperature imagery (2015-
737 2019) have been produced as part of the Multilayer Greenland Ice Surface Temperature, Surface Albedo,
738 and Water Vapor from MODIS V001 data set and are available at
739 https://doi.org/10.5067/7THUWT9NMPDK (Hall and DiGirolamo, 2019). OIB AR- and MCoRDS-derived
740 perennial firn aquifers detections (2010-2017) are available at
741 https://arcticdata.io/catalog/view/doi:10.18739/A2985M (Miège et al., 2016). OIB AR-derived ice slab
742 detections (2010-2014) are available at https://doi.org/10.6084/m9.figshare.8309777 (MacFerrin et al.,
743 2019). OIB AR-derived spatially coherent melt layer detections (2017) are available at
744 (https://doi.org/10.18739/A2736M33W) (Culberg et al., 2021). OIB AR L1B Geolocated Radar Echo
745 Strength Profiles, Version 2, are available at, https://doi.org/10.5067/0ZY1XYHNIQNY (Paden et al., 2018).
746 NASA MEaSUREs MODIS Mosaic of Greenland (MOG) 2015 Image Map, Version 2, is available at
747 https://nsidc.org/data/NSIDC-0547/versions/2 (Haran et al., 2018). SMAP-derived perennial firn aquifer and
748 ice slab extents are available at https://zenodo.org/record/5745983#.YabDdNDMKUk.

Author Contributions

750 JZM initiated the study, adapted the empirical model, performed the analyses, and wrote the manuscript.
751 RC processed and interpreted the OIB AR radargram profiles. All authors participated in discussions and
752 reviewed manuscript drafts.

Competing Interests

754 The authors declare that they have no conflict of interest.

Financial Support

JZM, DGL, and MJB are supported by the NASA SMAP Science Team (no. 80NSSC20K1806), and by the NASA Cryospheric Science Program (no. 80NSSC18K1055 and no. 80NSSC21K0749) under grants to the University of Colorado and Brigham Young University. RC is supported by a National Defense Science and Engineering Graduate Fellowship. RC and DMS are supported in part by NASA (no. NNX16AJ95G and NSF (no. 1745137). CAS is supported by NASA Headquarters Cryospheric Science Program. We acknowledge the use of data from CReSIS generated with support from the University of Kansas, NASA Operation IceBridge (no. NNX16AH54G), NSF (no. ACI-1443054, OPP-1739003, IIS-1838230), Lilly Endowment Incorporated, and Indiana METACyt Initiative.

References

Abdalati, W., and Steffen, K.: Snowmelt on the Greenland Ice Sheet as derived from passive microwave satellite data, J. Climate, 10, 165-175, https://doi.org/10.1175/1520-0442(1997)010<0165:SOTGIS>2.0.CO;2, 1997.

Alley, R. B., Dupont, T. K., Parizek, B. R., Anandakrishnan, S.: Access of surface meltwater to beds of sub-freezing glaciers: Preliminary insights, Ann. Glaciol., 40, 8-14, https://doi.org/10.3189/172756405781813483, 2005.

Ashcraft, I. and Long, D.: Comparison of methods for melt detection over Greenland using active and passive microwave measurements, Int. J. Remote Sens., 27, 2469-2488, https://doi.org/10.1080/01431160500534465, 2006.

Benson, C. S.: Stratigraphic studies in the snow and firn of the Greenland Ice Sheet, Ph.D. thesis, California Institute of Technology, 228 pp., 1960.

Brangers, I., Lievens, H., Miège, C., Demuzere, M., Brucker, L., and De Lannoy, G. J. M.: Sentinel-1 detects firn aquifers in the Greenland Ice Sheet, Geophys. Res. Lett., 47, e2019GL085192, https://doi.org/10.1029/2019GL085192, 2020.

Brodzik, M. J., Long, D. G., and Hardman, M. A.: SMAP Radiometer Twice-Daily rSIR-Enhanced EASE-Grid 2.0 Brightness Temperatures, Version 1, NASA National Snow and Ice Data Center Distributed Active Archive Center,https://doi.org/10.5067/QZ3WJNOUZLFK, 2019.

Brodzik, M. J., Billingsley, B., Haran, T., Raup, B., and Savoie, M. H.: EASE-Grid 2.0: Incremental but significant improvements for Earth-gridded data sets, ISPRS Int. J. Geo-Inf., 1, 32-45, https://doi.org/10.3390/ijgi1010032, 2012.

Chu, W., Schroeder, D. M., and Siegfried, M. R.: Retrieval of englacial firn aquifer thickness from ice-penetrating radar sounding in southeastern Greenland, Geophys. Res. Lett., 45, 11,770-11, 778, https://doi.org/10.1029/2018GL079751, 2018.

Chudley, T. R., Christoffersen, P., Doyle, S. H., Bougamont, M., Schoonman, C. M., Hubbard, B., James, M. R.: Supraglacial lake drainage at a fast-flowing Greenlandic outlet glacier,
Proc. Natl. Acad. Sci., 51, 25468-25477, https://doi.org/10.1073/pnas.1913685116, 2019.

CReSIS: CReSIS radar depth sounder data, Digital Media, http://data.cresis.ku.edu/, 2016.

Colgan, W., Rajaram, H., Abdalati, W., McCutchan, C., Mottram, R., Moussavi, M. S., and Grigsby, S.: Observations, models, and mass balance implications: Glacier crevasses, Rev. Geophys., 54, 119-161, https://doi.org/10.1002/2015RG000504, 2016.

Culberg, R., Schroeder, D.M. and Chu, W.: Extreme melt season ice layers reduce firn permeability across Greenland, Nat Commun, 12, 2336, https://doi.org/10.1038/s41467-021-22656-5, 2021

Culberg, R.: Refrozen melt layer location, density, and connectivity records from airborne radar sounding, Greenland, NSF Arctic Data Center, https://doi.org/10.18739/A2736M33W, 2021.

Cullather, R. I., Andrews, L. C., Croteau, M. J., Digirolamo, N. E., Hall, D. K., Lim, Y., Loomis, B. D., Shuman, C. A., and Nowicki, S. M. J.: Anomalous circulation in July 2019 resulting in mass loss on the Greenland Ice Sheet. Geophys. Res. Lett., 47, https://doi.org/10.1029/2020GL087263, 2020.

Das, S. B., Joughin, I., Behn, M. D., Howat, I. M., King, M. A., Lizarralde, D., Bhatia, M. P., Fracture propagation to the base of the Greenland Ice Sheet during supraglacial lake drainage, Science, 320, 778-781, https://doi.org/10.1126/science.1153360, 2008.

Dunmire, D., Banwell, A. F., Lenaerts, J. T. M., and Datta, R. T.: Contrasting regional variability of buried meltwater extent over two years across the Greenland Ice Sheet, The Cryosphere Discuss, https://doi.org/10.5194/tc-2021-3, in review, 2021.

Early, D. S., and Long, D. G.: Image reconstruction and enhanced-resolution imaging from irregular samples, IEEE Trans. Geosci. Remote Sens. 39, 291-302, https://doi.org/10.1109/36.905237, 2001.

Echelmeyer, K., Clarke, T. S., and Harrison, W. D.: Surficial glaciology of Jakobshavn Isbræ, West Greenland 1. Surface morphology, J. Glaciol., 37, 368–382, https://doi.org/10.1017/S0022143000005803, 1991.

Entekhabi, D., et al.: The Soil Moisture Active Passive (SMAP) Mission, Proc. IEEE, 98, 704-716, https://doi.org/10.1109/JPROC.2010.2043918, 2010.

Forster, R. R., Box, J. E., Van Den Broeke, M. R., Miège, C., Burgess, E. W., Van Angelen, J. H., Lenaerts, J. T. M., Koenig, L. S., Paden, J., Lewis, C., Gogineni, S. P., Leuschen, C., and McConnell, J. R.: Extensive liquid meltwater storage in firn within the Greenland Ice Sheet, Nat. Geosci., 7, 95–98, https://doi.org/10.1038/ngeo2043, 2014.

Fountain, A. G., and Walder, J. S.: Water flow through temperate glaciers. Rev. of Geophys., 36, 299-328, https://doi.org/10.1029/97RG03579, 1998.

Freilich, M. H., Long, D. G., and Spencer, M. W.: SeaWinds: A scanning scatterometer for ADEOS-II science overview, Proc. IEEE, 1994, 960-963, https://doi.org/10.1109/IGARSS.1994.399313, 1994.

Franco, B., Fettweis, X., and Erpicum, M.: Future projections of the Greenland ice sheet energy balance driving the surface melt, The Cryosphere, 7, 1–18, https://doi.org/10.5194/tc-7-1-2013, 2013

Hall, D. K., and DiGirolamo, N.: Multilayer Greenland Ice Surface Temperature, Surface Albedo, and Water Vapor from MODIS, Version 1, NASA National Snow and Ice Data Center Distributed Active Archive Center, https://doi.org/10.5067/7THUWT9NMPDK, 2019.

Hall, D. K., Comiso, J. C., Digirolamo, N. E., Shuman, C. A., Key, J. R., and Koenig, L. S.: A satellite-derived climate-quality data record of the clear-sky surface temperature of the Greenland Ice Sheet, J. Clim., 25, 4785–4798, https://doi.org/10.1175/JCLI-D-11-00365.1, 2012.

Haran, T., Bohlander J., Scambos T., Painter, T., and Fahnestock, M.: MEaSUREs MODIS Boulder, Colorado USA. NASA National Snow and Ice Data Center Distributed Active Archive Center, https://doi.org/10.5067/9ZO79PHOTYE5, 2018.

Harper, J., Humphrey, N., Pfeffer, W. T., Brown, J., and Fettweis, X.: Greenland ice-sheet contribution to sea-level rise buffered by meltwater storage in firn, Nature, 491, 240–243, https://doi.org/10.1038/nature11566, 2012.

Hicks, B. R., and Long, D. G.: Inferring Greenland melt and refreeze severity from SeaWinds scatterometer data, Int. J. Remote Sensing, 32, 8053-8080, https://doi.org/10.1080/01431161.2010.532174, 2011.

Howat, I.: MEaSUREs Greenland Ice Mapping Project (GIMP) Land Ice and Ocean Classification Mask, Version 1, NASA National Snow and Ice Data Center Distributed Active Archive Center, https://doi.org/10.5067/B8X58MQBFUPA, 2017.

Howat, I., Negrete, A., and Smith, B.: MEaSUREs Greenland Ice Mapping Project (GIMP) Digital Elevation Model, Version 1, NASA National Snow and Ice Data Center Distributed Active Archive Center, doi: https://doi.org/10.5067/NV34YUIXLP9W, 2015.

Howat, I., Negrete, A., and Smith, B.: The Greenland Ice Mapping Project (GIMP) land classification and surface elevation datasets, The Cryosphere, 8, 1509-1518, https://doi.org/10.5194/tc-8-1509-2014, 2014.

Humphrey, N. F., Harper, J. T., and Pfeffer, W. T.: Thermal tracking of meltwater retention in Greenland's accumulation area, J. Geophys. Res., 117, https://doi.org/10.1029/2011JF002083, 2012.

Jezek, K. C., Gogineni, P., and Shanableh, M.: Radar measurements of melt zones on the Greenland Ice Sheet, Geophys. Res. Lett., 21, 33-36, https://doi.org/10.1029/93GL03377, 1994.

Jezek, K. C., Johnson, J. T., Drinkwater, M. R., Macelloni, G., Tsang, L., Aksoy, M., and Durand M.: Radiometric approach for estimating relative changes in intraglacier average temperature, IEEE Trans. Geosci. Remote Sens., 53, 134-143, https://doi.org/10.1109/TGRS.2014.2319265, 2015.

Jezek, K. C., Johnson J. T., Tan S., Tsang L., Andrews, M. J., Brogioni, M., Macelloni, G., Durand, M., Chen, C. C., Belgiovane, D. J., Duan, Y., Yardim, C., Li, H., Bringer, A., Leuski, V., and Aksoy, M.: 500–2000-MHz brightness temperature spectra of the northwestern Greenland Ice Sheet, IEEE Trans. Geosci. Remote Sens., 56, 1485-1496, https://doi.org/10.1109/TGRS.2017.2764381, 2018.

Joughin, I., Das, S. B., Flowers, G .E., Behn, M. D., Alley, R. B., King, M. A., Smith, B. E., Bamber, J. L., van den Broeke, M. R., and Van Angelen, J. H.: Influence of ice-sheet geometry and supraglacial lakes on seasonal ice-flow variability, The Cryosphere, 7, 1185-1192, https://doi.org/10.5194/tc-7-1185-2013, 2013.

Joughin, I., Das, S. B., King, M. A., Smith, B. E., Howat, I. M., and Moon, T.: Seasonal speedup along the western flank of the Greenland Ice Sheet, Science, 320, 781-783, https://doi.org/10.1126/science.1153288, 2008.

Kerr, Y. H., Waldteufel, P., Wigneron, J., Martinuzzi, J., Font, J., and Berger, M.: Soil moisture retrieval from space: The Soil Moisture and Ocean Salinity (SMOS) mission, IEEE Trans. Geosci. Remote Sens., 39, 1729-1735, https://doi.org/10.1109/36.942551, 2001.

Koenig, L. S., Miège, C., Forster, R. R., and Brucker, L.: Initial in situ measurements of perennial meltwater storage in the Greenland firn aquifer, Geophys. Res. Lett., 41, 81-85, https://doi.org/10.1002/2013GL058083, 2014.

Koenig, L. S., Lampkin, D. J., Montgomery, L. N., Hamilton, S. L., Turrin, J. B., Joseph, C. A., Moutsafa, S. E., Panzer, B., Casey, K. A., Paden, J. D., Leuschen, C., and Gogineni, P.: Wintertime storage of water in buried supraglacial lakes across the Greenland Ice Sheet, The Cryosphere, 9, 1333–1342, https://doi.org/10.5194/tc-9-1333-2015, 2015.

Kuipers Munneke, P. K., Ligtenberg, S. R. M., Van Den Broeke, M. R., Van Angelen, J. H., and Forster, R. R.: Explaining the presence of perennial liquid water bodies in the firn of the Greenland Ice Sheet, Geophys. Res. Lett., 41, 476–483, https://doi.org/10.1002/2013GL058389, 2014.

Le Vine, D. M., Lagerloef, G. S. E., and Torrusio, S. E.: Aquarius and remote sensing of sea surface salinity from space, Proc. IEEE, 98, 688-703, https://doi.org/10.1109/JPROC.2010.2040550, 2010.

Lewis, C., Gogineni, S., Rodriguez-Morales, F., Panzer, B., Stumpf, T., Paden, J., and Leuschen, C.: Airborne fine-resolution UHF radar: An approach to the study of englacial reflections, firn compaction and ice attenuation rates, J. Glaciology, 61, 89-100. https://doi.org/10.3189/2015JoG14J089, 2015.

Long, D. G., Brodzik, M. J., and Hardman M. A.: Enhanced-resolution SMAP brightness temperature image products, IEEE Trans. Geosci. Remote Sens., 57, 4151-4163, https://doi.org/10.1109/TGRS.2018.2889427, 2019.

Long, D. G., and Brodzik, M. J.: Optimum image formation for spaceborne microwave radiometer products, IEEE Trans. Geosci. Remote Sens., 54, 2763-2779. https://doi.org/10.1109/TGRS.2015.2505677, 2016.

Long, D. G., and Daum, D. L.: Spatial resolution enhancement of SSM/I data, IEEE Trans. Geosci. Remote Sens., 36, 407-417, https://doi.org/10.1109/36.662726, 1998.

Long, D. G., Hardin, P. J., and Whiting, P. T.: Resolution enhancement of spaceborne scatterometer data, IEEE Trans. Geosci. Remote Sens., 31, 700-715, https://doi.org/10.1109/36.225536, 1993.

MacFerrin, M., Machguth, H., van As, D., Charalampidis, C., Stevens, C. M., Heilig, A., Vandecrux, B., Langen, P. L., Mottram, R., Fettweis, X., van den Broeke, M. R., Pfeffer, W. T., Moussavi, M. S., and Abdalati, W.: Rapid expansion of Greenland's low-permeability ice slabs. Nature, 573, 403-407, https://doi.org/10.1038/s41586-019-1550-3, 2019.

Machguth, H. MacFerrin M., van As, D., Box, J. E., Charalampidis, C., Colgan., W., Fausto, R. S., Harro, A. J., Mosley-Thompson, E., and van de Wal, R. S. W.: Greenland meltwater storage in firn limited by near-surface ice formation. *Nat. Clim. Chang.* 6, 390-393, https://doi.org/10.1038/nclimate2899, 2016.

Mätzler, C., and Hüppi, R.: Review of signature studies for microwave remote sensing of snowpacks, Adv. in Space Res., 9, 253-265, https://doi.org/10.1016/0273-1177(89)90493-6, 1989.

Miège, C., Forster, R. R., Brucker, L., Koenig, L. S., Solomon, D.K., Paden, J. D., Box, J. E., Burgess, E. W., Miller, J. Z., McNerney, L., Brautigam, N., Fausto, R. S., and Gogineni, S.: Spatial extent and temporal variability of Greenland firn aquifers detected by ground and airborne radars, J. Geophys. Res. Earth, 121, 2381–2398, https://doi.org/10.1002/2016JF003869, 2016.

Miles, K. E., Willis, I. C., Benedek, C. L., Williamson, A. G., and Tedesco, M.: Toward monitoring surface and subsurface lakes on the Greenland Ice Sheet Using Sentinel-1 SAR and Landsat-8 OLI imagery, Frontiers in Earth Science, 5, 58, https://doi.org/https://doi.org/10.3389/feart.2017.00058, 2017.

Miller, J. Z., Long, D. G., Jezek, K. C., Johnson, J. T., Brodzik, M. J., Shuman, C. A., Koenig, L. S., and Scambos, T. A.: Brief communication: Mapping Greenland's perennial firn aquifers using enhanced-resolution L-band brightness temperature image time series, The Cryosphere, 14, 2809–2817, https://doi.org/10.5194/tc-14-2809-2020, 2020.

Miller, J. Z.: Mapping Greenland's firn aquifers from space using active and passive satellite microwave remote sensing, Ph.D. thesis, Department of Geography, University of Utah, 135 pp., 2019.

Miller, O. L., Solomon, D. K., Miège, C., Koenig, L. S., Forster, R. R., Montgomery, L. N., Schmerr, N., Ligtenberg, S. R. M., Legchenko, A., and Brucker, L.: Hydraulic conductivity of a firn aquifer in southeast Greenland, Front. Earth Sci., 5, https://doi.org/10.3389/feart.2017.00038, 2017.

Montgomery, L. N., Schmerr, N., Burdick, S., Forster, R. R., Koenig, L., Legchenko, A., Ligtenberg, S., Miège, C., Miller, O. L., and Solomon, D. K.: Investigation of firn aquifer structure in southeastern Greenland using active source seismology, Front. Earth Sci., 5, https://doi.org/10.3389/feart.2017.00010, 2017.

Moon, T., Joughin, I., Smith, B., Broeke, M. R., Berg, W. J., Noël, B., and Usher, M.: Distinct patterns of seasonal Greenland glacier velocity, Geophys. Res. Lett., 41, 7209-7216, https://doi.org/10.1002/2014GL061836, 2014.

Mote, T. L., and Andersen, M. R.: Variations in snowpack melt on the Greenland Ice Sheet based on passive microwave measurements, J. Glaciology, 41, 51-60, https://doi.org/10.1017/S0022143000017755, 1995.

Müller, F.: Zonation in the Accumulation Area of the Glaciers of Axel Heiberg Island, N.W.T., Canada, J. of Glaciology, 4, 302-311, 1962.

Noël, B., van Kampenhout, L., Lenaerts, J. T. M., van de Berg, W. J, and van den Broeke, M. R.: A 21st century warming threshold for sustained Greenland Ice Sheet mass loss, Geophys. Res. Lett.,, 48(5), https://doi.org/10.1029/2020GL090471, 2021.

Noël, B., van de Berg, Willem Jan, Lhermitte, S. L. M., and van den Broeke, Michiel R.: Rapid ablation zone expansion amplifies north Greenland mass loss, Sci. Adv., 5, eaaw0123, https://doi.org/10.1126/sciadv.aaw0123, 2019.

Nghiem, S.V., Steffen, K., Neumann, G.A., and Huff, R: Mapping of ice layer extent and snow accumulation in the percolation zone of the Greenland ice sheet, J. Geophys. Res., 110, https://agupubs.onlinelibrary.wiley.com/doi/full/10.1029/2004JF000234. 2005.

Nghiem, S. V., Hall, D. K., Mote, T. L., Tedesco, M., Albert, M. R., Keegan, K., Shuman, C. A., DiGirolamo, N.E., and Neumann, G.: The extreme melt across the Greenland Ice Sheet in 2012, Geophys. Res. Lett., 39, L20502, https://doi.org/10.1029/2012GL053611, 2012.

Paden, J., Li, J., Leuschen C., F. Rodriguez-Morales, F., and Hale, R.: IceBridge Accumulation Radar L1B Geolocated Radar Echo Strength Profiles, Version 2, NASA National Snow and Ice Data Center Distributed Active Archive Center, https://doi.org/10.5067/0ZY1XYHNIQNY, 2014, updated 2018.

Pfeffer, W. T., Meier, M. F., and Illangasekare, T. H.: Retention of Greenland runoff by refreezing: Implications for projected future sea level change. J. Geophys. Res. Oceans, 96, 22117-22124, https://doi.org/10.1029/91JC0250, 1991.

Pfeffer, W. T., and Humphrey, N.F.: Determination of timing and location of water movement and ice-layer formation by temperature measurements in sub-freezing snow, J. Glaciol., 42, 292-304, https://doi.org/10.1017/S0022143000004159, 1996.

Piepmeier, J. R., et al.: SMAP L-band microwave radiometer: Instrument design and first year on orbit. IEEE Trans. Geosci. Remote Sens, 55, 1954-1966, https://doi.org/10.1109/TGRS.2016.2631978, 2017.

Poinar, K., Joughin, I., Lilien, D., Brucker, L., Kehrl, L., and Nowicki, S.: Drainage of southeast Greenland firn aquifer water through crevasses to the bed. Front. Earth Sci., https://doi.org/10.3389/feart.2017.00005, 2017.

Poinar, K., Dow, C. F., and Andrews, L. C.: Long-term support of an active subglacial hydrologic system in southeast Greenland by firn aquifers. Geophys. Res. Lett., 46, 4772-4781, https://doi.org/10.1029/2019GL082786, 2019.

Rignot, E.: Backscatter model for the unusual radar properties of the Greenland Ice Sheet, J. Geophys. Res. Planets, 100, 9389–9400, https://doi.org/10.1029/95JE00485, 1995.

1024 Rignot, E. J., Ostro, S. J., Van Zyl, J., and Jezek, K. C.: Unusual radar echoes from the Greenland Ice
1025 Sheet, Science, 261, 1710-1713, https://doi.org/10.1126/science.261.5129.171, 1993.
1026
1027 Rodriguez-Morales, F., et al.: Advanced multi-frequency radar instrumentation for polar research, IEEE
1028 Trans. Geosci. Remote Sens., 52, 2824-2842, https://doi.org/10.1109/TGRS.2013.2266415, (2014).
1029
1030 Schröder L., Neckel N., Zindler R., Humbert A.: Perennial supraglacial lakes in northeast Greenland
1031 observed by polarimetric SAR, Remote Sensing, 12, 2798, https://doi.org/10.3390/rs12172798 (2020).
1032
1033 Shuman, C. A., Hall, D. K., DiGirolamo, N. E., Mefford T. K., and Schnaubelt, M. J.: Comparison of near-
1034 surface air temperatures and MODIS ice-surface temperatures at Summit, Greenland (2008–2013), J. Appl.
1035 Meteor. Climatol., 53, 2171-2180, https://doi.org/10.1175/JAMC-D-14-0023.1, 2014.
1036
1037 Steffen, K., Nghiem, S. V., Huff, R., and Neumann, G.: The melt anomaly of 2002 on the Greenland Ice
1038 Sheet from active and passive microwave satellite observations. Geophys. Res. Lett., 31, L2040,
1039 https://doi.org/10.1029/2004GL020444, 2004.
1040
1041 Stevens, L. A., Behn, M. D., McGuire, J. J., Das, S. B., Joughin, I., Herring, T., Shean, D. E., and King, M.
1042 A.: Greenland supraglacial lake drainages triggered by hydrologically induced basal slip, Nature, 522, 73-
1043 76. https://doi.org/10.1038/nature14480, 2015.
1044
1045 Swift, C. T., Hayes, P. S., Herd, J. S., Jones, W. L., and Delnore, V. E.: Airborne microwave measurements
1046 of the southern Greenland Ice Sheet, J. Geophys. Res. Solid Earth, 90, 1983-1994,
1047 https://doi.org/10.1029/JB090iB02p01983, 1985.
1048
1049 Tedesco, M., and Fettweis, X.: Unprecedented atmospheric conditions (1948–2019) drive the 2019
1050 exceptional melting season over the Greenland Ice Sheet, The Cryosphere, 14, 1209-1223,
1051 https://doi.org/10.5194/tc-14-1209-2020, 2020.
1052
1053 Tedesco, M., Mote, T., Fettweis, X., Hanna, E., Jeyaratnam, J., Booth, J. F., Datta, R., and Briggs, K.: Arctic
1054 cut-off high drives the poleward shift of a new Greenland melting record, Nature Commun., 7, 11723-11723,
1055 https://doi.org/10.1038/ncomms11723 1985, 2016.
1056
1057 Tedesco, M., Fettweis, X., van den Broeke, M. R., van de Wal, R. S. W., Smeets, C. J. P. P., van de Berg,
1058 W. J., Serreze, M. C., and Box, J. E.: The role of albedo and accumulation in the 2010 melting record in
1059 Greenland, Environ. Res. Lett, 6, 014005, https://doi.org/10.1088/1748-9326/6/1/014005, 2011.
1060
1061 Tedesco, M., Serreze, M., and Fettweis, X.: Diagnosing the extreme surface melt event over southwestern
1062 Greenland in 2007. The Cryosphere, 2, 159-166. https://doi.org/10.5194/tc-2-159-2008, 2008.
1063
1064 Tiuri, M. E., Sihvola, A. H., Nyfors, E. G., Hallikaiken, M. T.: The complex dielectric constant of snow at
1065 microwave frequencies, IEEE J. Ocean Eng, 9, 377-382, https://doi.org/10.1109/JOE.1984.1145645, 1984.
1066
1067 Tsai, W., Nghiem, S. V., Van Zyl, J. J.: SeaWinds scatterometer on QuikSCAT mission and the emerging
1068 land and ocean applications, Proc. SPIE 4152, https://doi.org/10.1117/12.410586, 2000.
1069
1070 Turton, J. V., Hochreuther, P., Reimann, N., and Blau, M. T.: The distribution and evolution of supraglacial
1071 lakes on the 79° N Glacier (northeast Greenland) and interannual climatic controls, The Cryosphere
1072 Discuss, https://doi.org/10.5194/tc-2021-45, in review, 2021.
1073
1074 Ulaby, F. T., Long, D. G., Blackwell, W. J., Elachi, C., Fung, A. K., Ruf, C., Sarabandi, C., Zebker, H. A.,
1075 Van Zyl, J.: Microwave radar and radiometric remote sensing, University of Michigan Press, Ann Arbor,
1076 2014.
1077

1078   van den Broeke, M. R., Enderlin, E. M., Howat, I. M., Kuipers Munneke, P., Noël, B. P. Y., van de Berg, W.
1079   J., van Meijgaard, E., and Wouters, B.: On the recent contribution of the Greenland ice sheet to sea level
1080   change, The Cryosphere, 10, 1933–1946, https://doi.org/10.5194/tc-10-1933-2016, 2016.
1081

1082   van der Veen, C. J.: Fracture propagation as means of rapidly transferring surface meltwater to the base
1083   of glaciers, Geophys. Res. Lett., 34, L01501, https://doi.org/10.1029/2006GL028385, 2005.
1084

1085   Wessel, P., and Smith, W. H. F.: A global, self-consistent, hierarchical, high-resolution shoreline database,
1086   J. Geophys. Res., 101, 8741–8743, https://doi.org/10.1029/96JB00104, 1996.
1087

1088   Zwally, H. J., Abdalati, W., Herring, T., Larson, K., Saba, J., and Steffen, K.: Surface melt-induced
1089   acceleration of Greenland Ice Sheet flow, Science, 297, 218-222, https://doi.org/10.1126/science.1072708,
1090   2002.
1091

1092   Zwally, J. H.: Microwave emissivity and accumulation rate of polar firn, J. Glaciol., 18, 195-215,
1093   https://doi.org/10.1017/S0022143000021304, 1977.
1094
1095
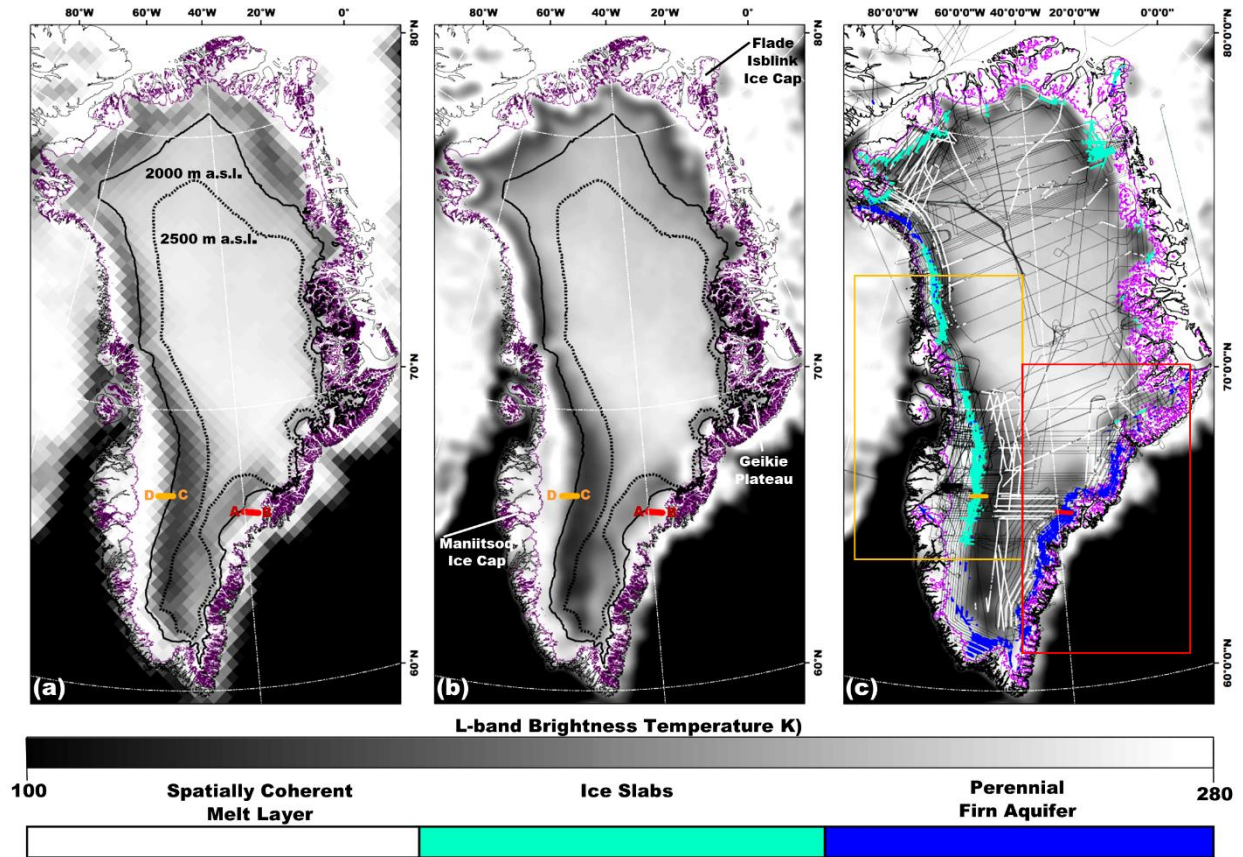
1096

Figure 1

(a) Gridded (25 km gridding, 30 km effective resolution), and (b) enhanced-resolution (3.125 km gridding, 18 km effective resolution) L-band T_V^B imagery generated using observations collected 15 April 2016 by the microwave radiometer on the SMAP satellite during the evening orbital pass interval over Greenland (Long et al., 2019) overlaid with the 2000 m a.s.l. contour (black line), and the 2500 m a.s.l. contour (dotted black line; Howat et al., 2014); the ice sheet extent (purple line; Howat et al., 2014); and the coastline (black peripheral line; Wessel and Smith, 1996). (c) SMAP enhanced-resolution L-band T_V^B imagery overlaid with AR- and MCoRDS-derived 2010-2017 perennial firn aquifer (blue shading; Miège et al., 2016), 2010-2014 ice slab (cyan shading; MacFerrin et al., 2019), and 2012 spatially coherent melt layer (white shading; Culberg et al., 2021) detections along OIB flight lines (black interior lines); zoom areas over south eastern Greenland (red box; Fig. 2a), and south western Greenland (orange box; Fig. 2b); and AR radargram transect A-B (red line; Fig. 3a) and C-D (orange line; Fig. 3b).
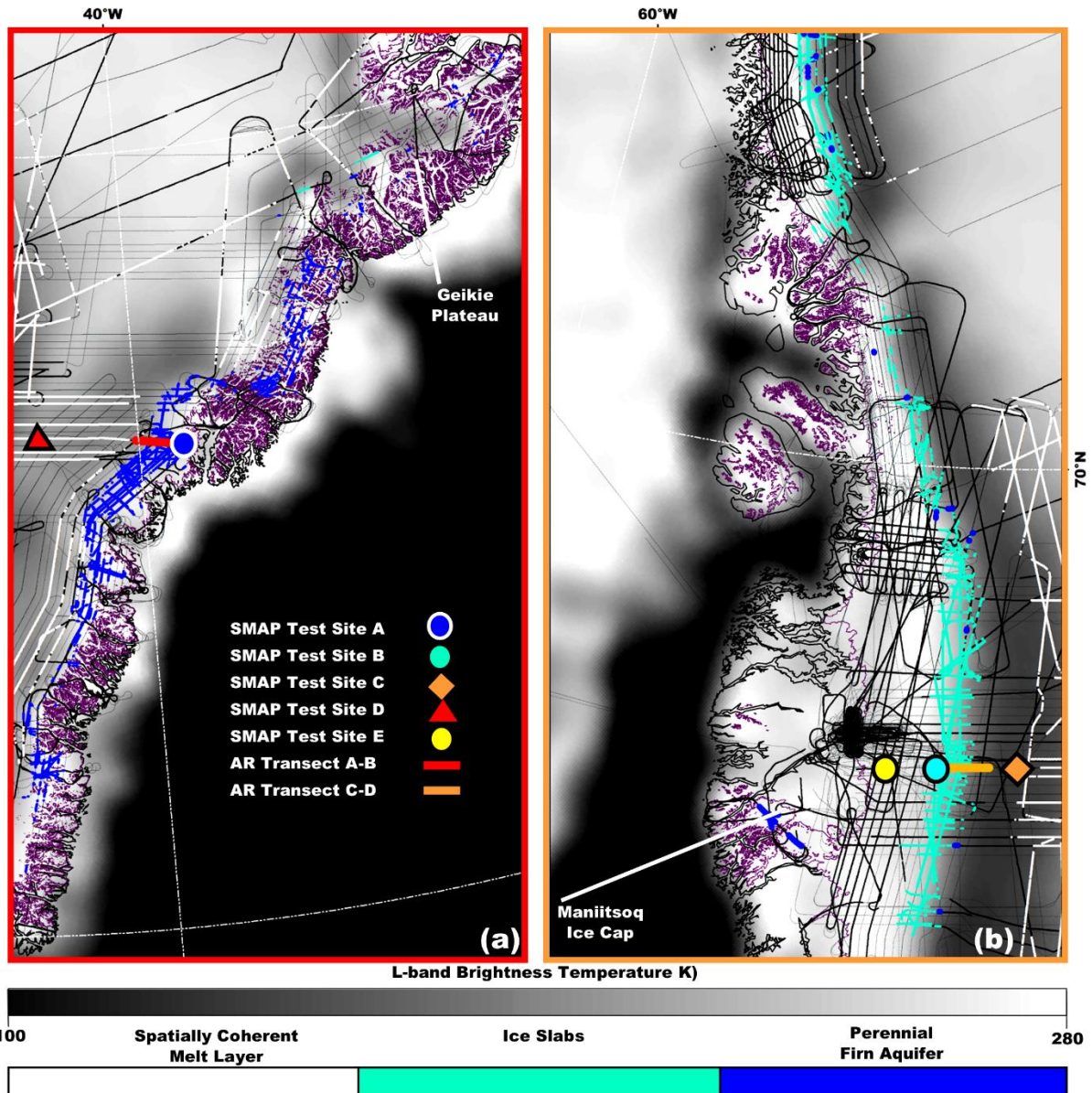
Figure 2

Enhanced-resolution (3.125 km gridding, 30 km effective resolution) L-band T_V^B imagery generated using observations collected 15 April 2016 by the microwave radiometer on the SMAP satellite during the evening orbital pass interval over (a) south eastern Greenland (red box, Fig. 1c), and (b) south western Greenland (orange box, Fig. 1c,) (Long et al., 2019) overlaid with the ice sheet extent (purple line; Howat et al., 2014); the coastline (black peripheral line; Wessel and Smith, 1996); the AR- and MCoRDS-derived 2010-2017 perennial firn aquifer (blue shading; Miège et al., 2016), 2010-2014 ice slab (cyan shading; MacFerrin et al., 2019), and 2012 spatially coherent melt layer (white shading; Culberg et al., 2021) detections along OIB flight lines (black interior lines); AR radargram transect A-B (red line; Fig. 3a), and C-D (orange line; Fig. 3b); and SMAP Test Site A (blue circle; Fig. 4a), B (cyan circle; Fig. 4b), C (orange diamond; Fig. 4c), D (red triangle; Fig. 4d), and E (yellow circle; Fig. 4e).
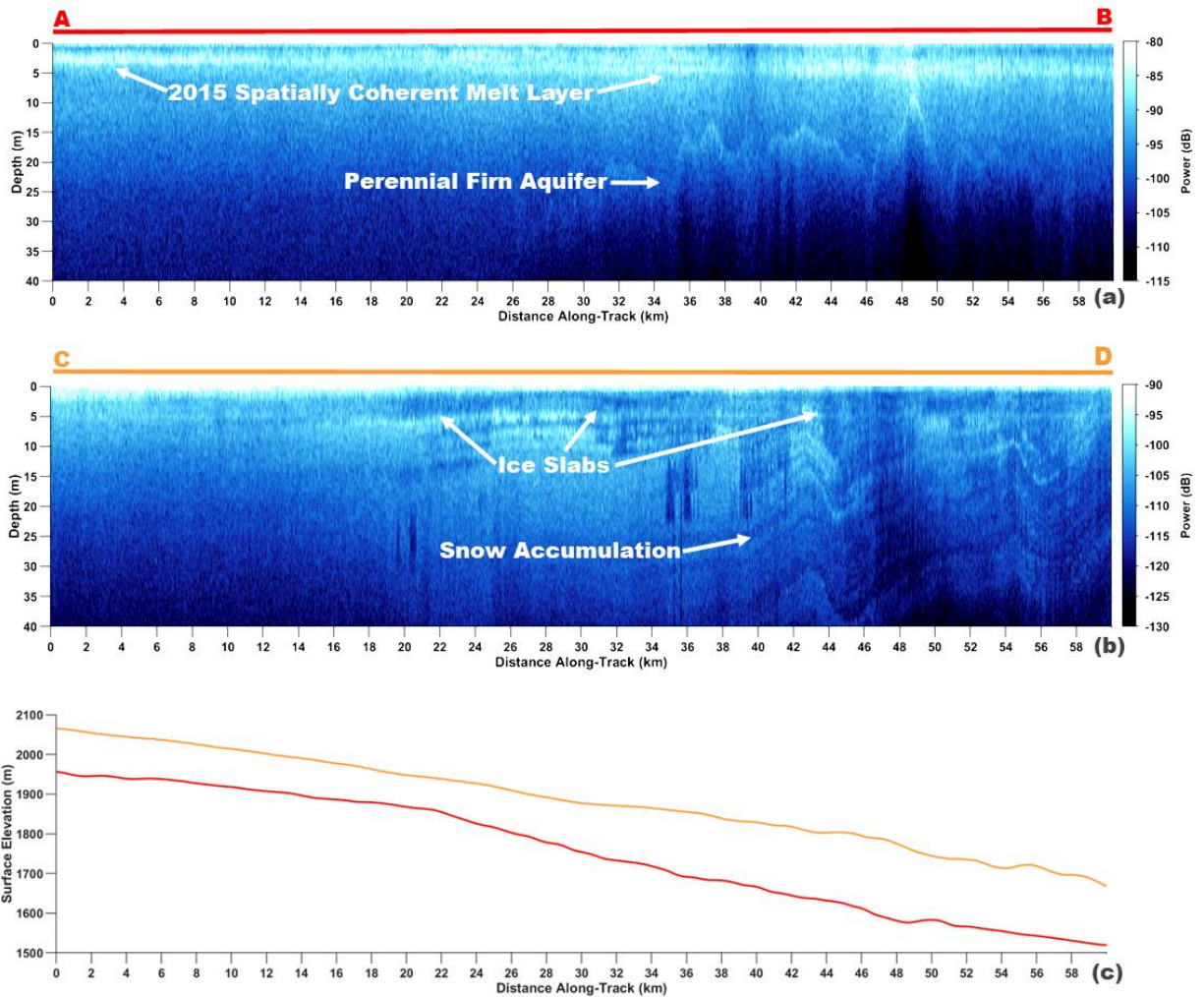
Figure 3

AR radargram transect (a) A-B (red line, Fig. 2a) collected on 22 April 2017, and (b) C-D (orange line, Fig. 2b) collected on 5 May 2017 (Rodriguez-Morales et al, 2014). (c) AR radargram transect A-B (red line), and C-D (orangle line) elevation profiles. The exceptionally bright upper surface-parallel reflector in (a) is a spatially coherent melt layer. The bright lower reflector in (a) is the upper surface of meltwater stored within a perennial firn aquifer. The thick dark surface-parallel regions of low-reflectivity in (b) are ice slabs. The alternating sequences of bright and dark surface-parallel reflectors in (b) are seasonal snow accumulation layers.
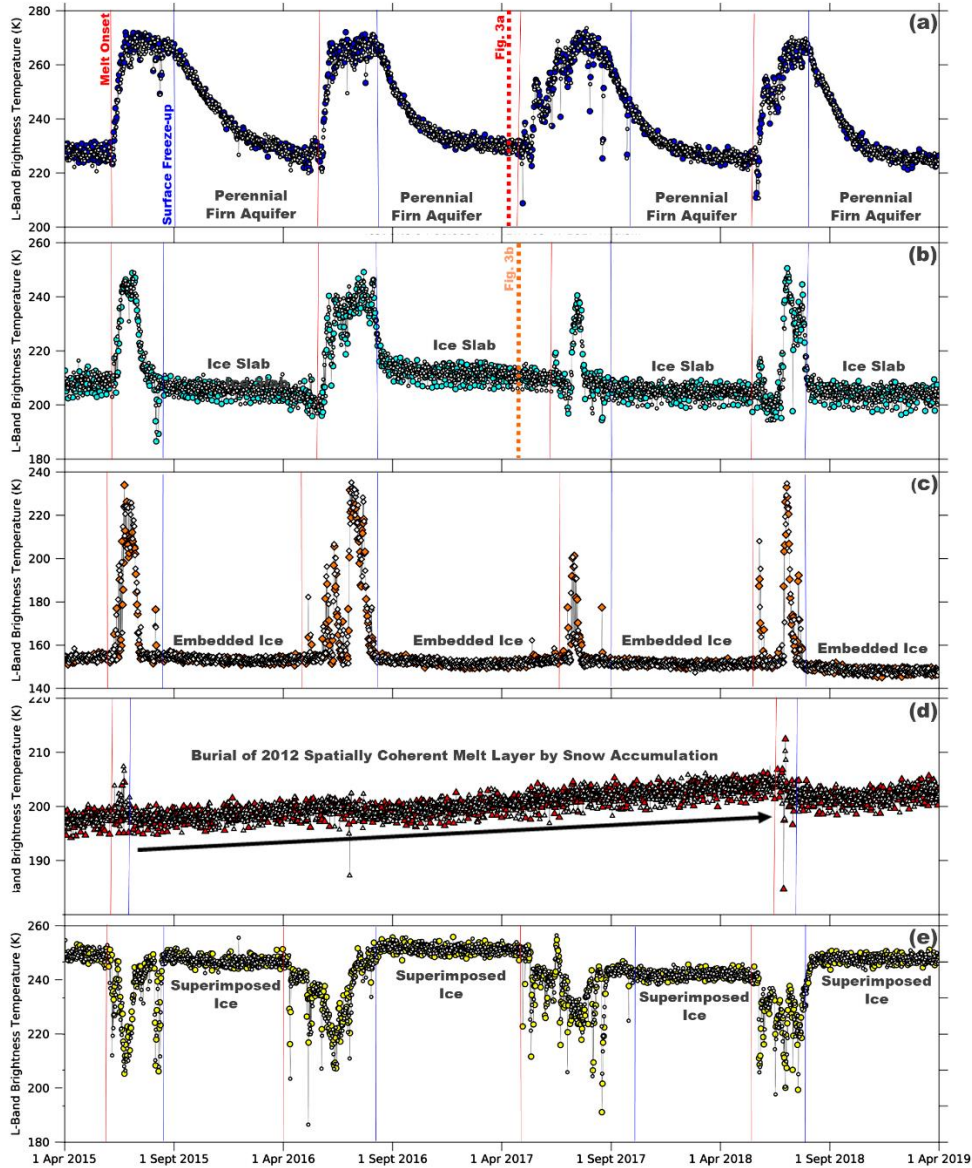
1130

Figure 4

Temporal L-band signatures that alternate morning (white symbols) and evening (colored symbols) orbital pass interval enhanced-resolution T_V^B generated using observations collected over the GrIS by the microwave radiometer on the SMAP satellite (Long et al., 2019) over (a) SMAP Test Site A (blue circles; Fig. 2a), (b) B (cyan circles; Fig. 2b), (c) C (orange diamonds; Fig 2b), (d) D (red triangles; Fig. 2a), and (e) E (yellow circles; Fig. 2b). Melt onset (red lines) and surface freeze-up (blue lines) dates derived from thermal infrared T^B collected by MODIS on the Terra and Aqua satellites (Hall et al, 2012). AR radargram transect A-B (red dashed line; Figs. 3a) collected on 22 April 2017, and C-D (orange dashed line; Fig. 3b) collected on 5 May 2017.
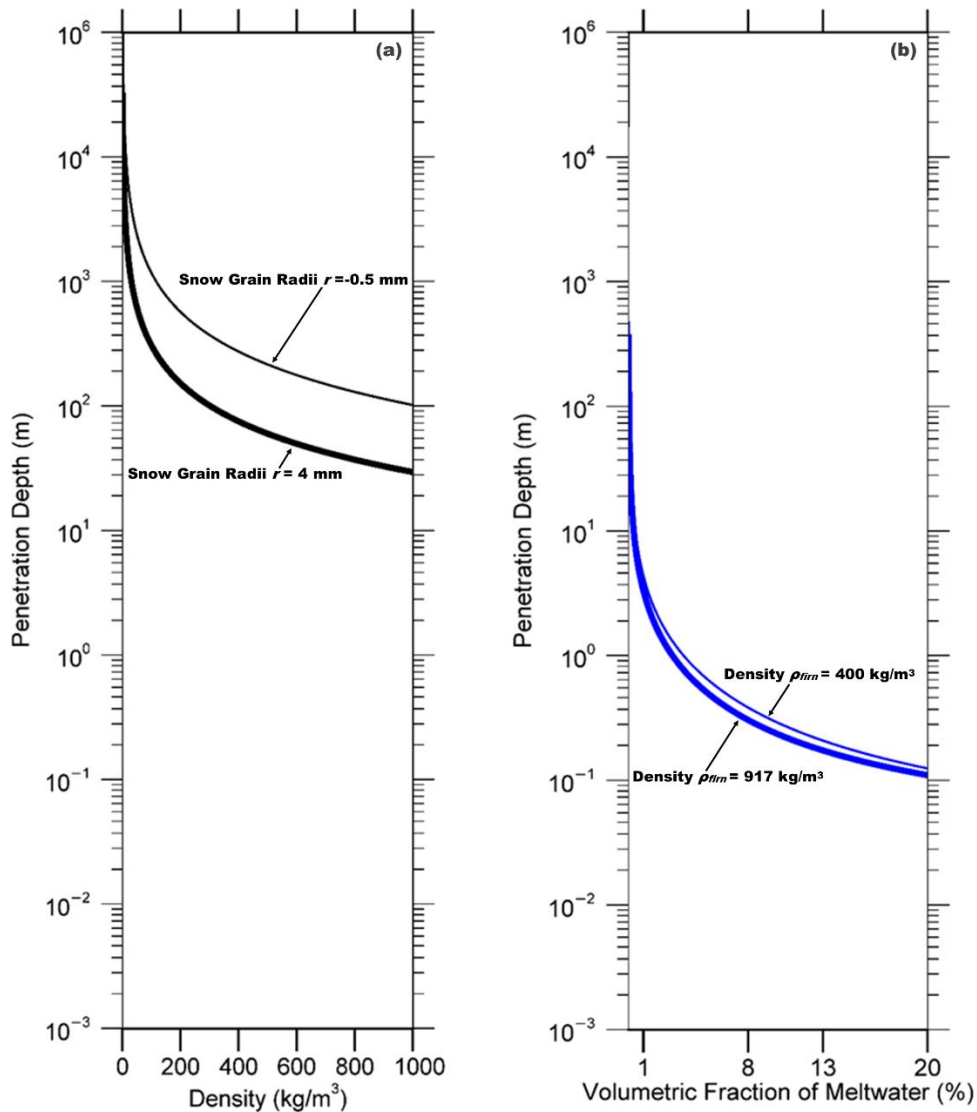
1140

1141   **Figure 5**

1142   *Theoretical L-band penetration depths for of uniform layer of (a) refrozen, and (b) water-saturated firn.*

1143   *Penetration depths $\left(\frac{1}{\kappa_s+\kappa_a}\right)$ are calculated as a function of the Raleigh scattering coefficient (κ_s; Eq. 8), and*

1144   *the absorption coefficient (κ_a; Eq. 10). The complex dielectric constant is calculated using the empirically*

1145   *derived models described in Tiuri et al., (1984). Refrozen firn penetration depths are calculated as a function*

1146   *of firn density (ρ_{firn}), and the curves are plotted for snow grain radii (r) set to $r=0.5$ mm (upper curve), and*

1147   *$r=4$ mm (lower curve). Water-saturated firn penetration depths are calculated as a function of the volumetric*

1148   *fraction of meltwater (m_v), and the curves are plotted for firn density set to $\rho_{firn}=400$ kg/m³ (upper curve),*

1149   *and $\rho_{firn}=917$ kg/m³ (lower curve). Given the complexity of modeling embedded ice structures, they are*

1150   *excluded from the penetration depth calculation. Increases in the volumetric fraction of embedded ice within*

1151   *the firn will result in an increase in volume scattering, which will decrease and compress the distance*

1152   *between the penetration depth curves for both refrozen and water-saturated firn.*
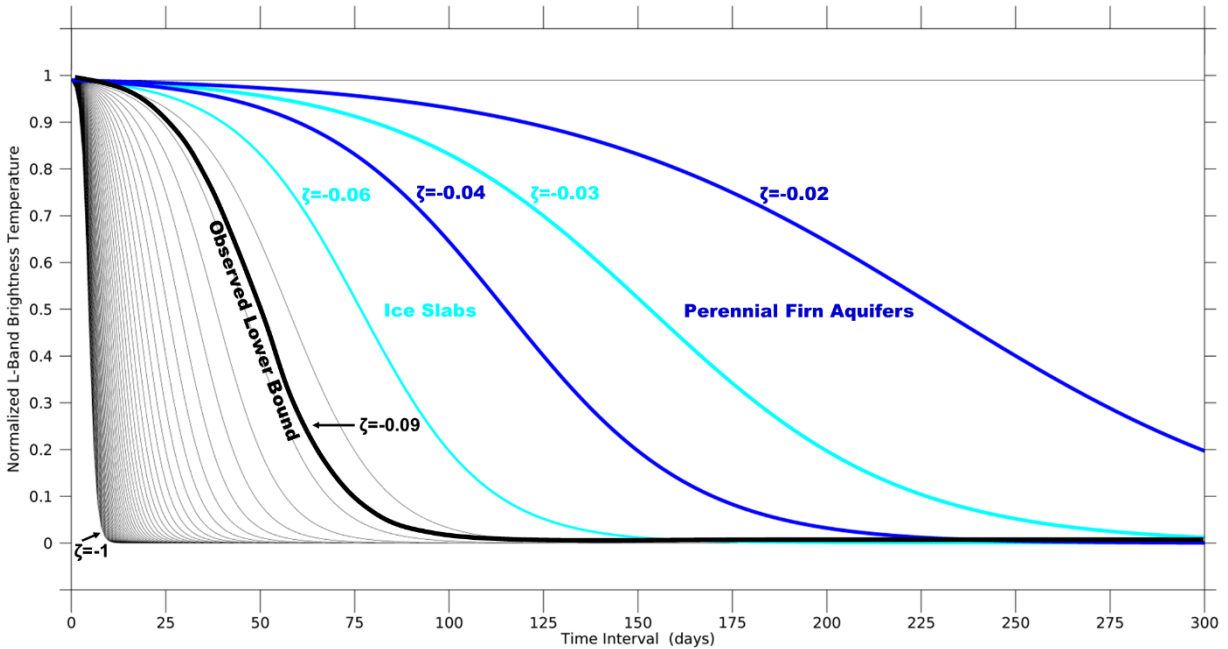
1153

Figure 6

Example set of simulated sigmoidal curves that represent our model of the exponentially decreasing temporal L-band signatures predicted over the percolation facies. The initial normalized vertically-polarized L-band brightness temperature was fixed at a value of $T_{V,N}^{B}(t_{max})$ = 0.99, and the time interval was set to a value of $t \in [\, t_{max}, t_{min}] = 300$ observations. The refreezing rate parameter was set to values between $\zeta = [\, -1,\, 0\,]$ incremented by steps of 0.02. The blue lines correspond to the interval $\zeta \in [\, -0.04,\, -0.02\,]$ and produce curves similar to those observed over perennial firn aquifer areas. The cyan lines correspond to the interval $\zeta \in [-0.06,\, -0.03\,]$ and produce curves similar to those observed over ice slab areas. The black line is the observed lower bound ($\zeta = -0.09$) of the refreezing rate parameter of partitioned T_{V}^{B} time series iteratively fit to the sigmoid function (Section 2.3.4).
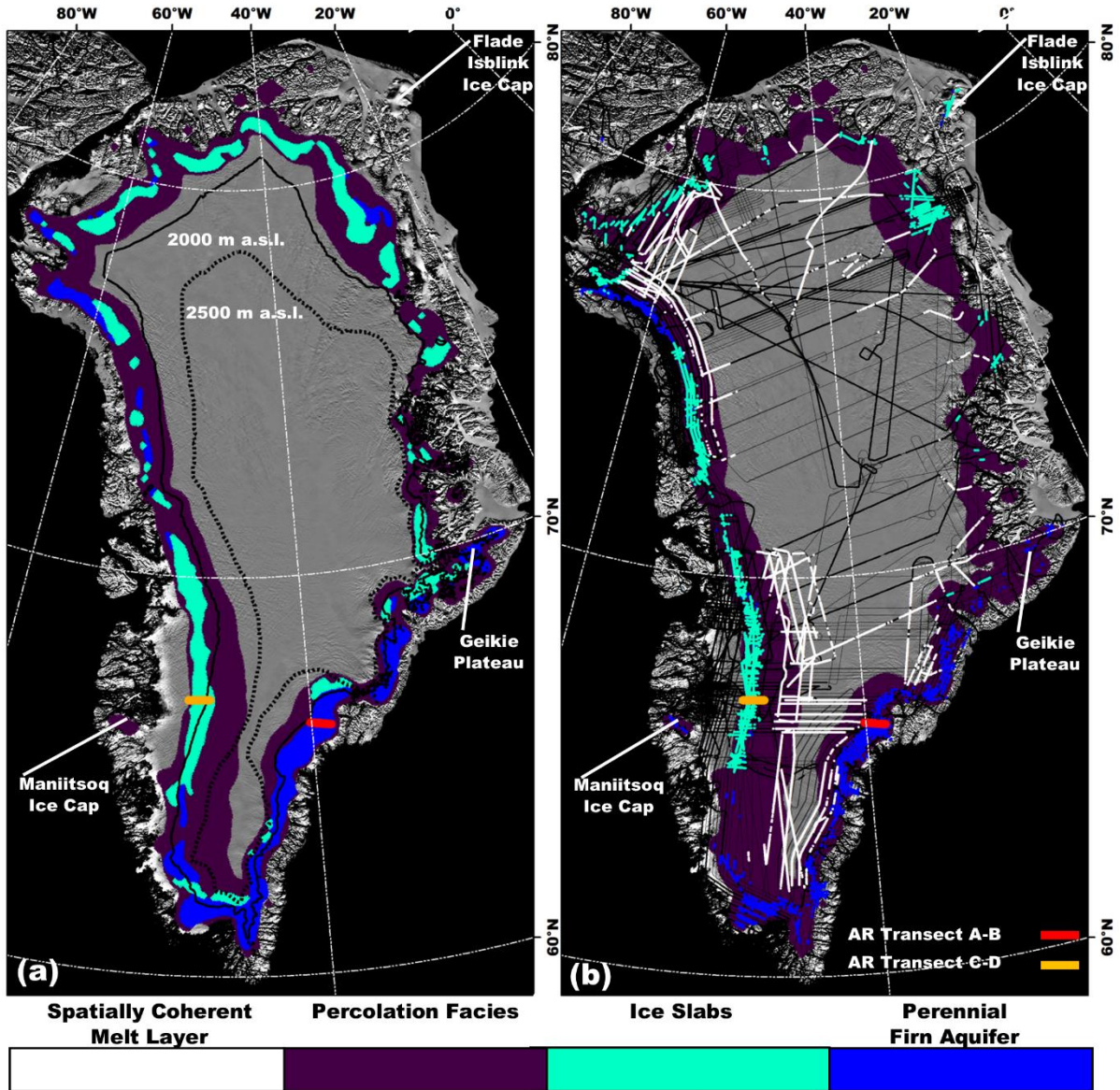
1167

1168   **Figure 7**

1169   *(a) SMAP-derived perennial firn aquifer (blue shading), ice slab (cyan shading), and percolation facies*
1170   *(purple shading) extents (2015-2019) generated by the adapted empirical algorithm; and the 2000 m a.s.l.*
1171   *contour (black line), and the 2500 m a.s.l. contour (black dotted line; Howat et al., 2014) overlaid on the*
1172   *2015 MODIS Mosaic of Greenland (MOG) image map (Haran et al., 2018). (b) SMAP-derived extents are*
1173   *overlaid with AR- and MCoRDS-derived 2010-2017 perennial firn aquifer (blue shading; Miège et al., 2016),*
1174   *2010-2014 ice slab (cyan shading; MacFerrin et al., 2019), and 2012 spatially coherent melt layer (white*
1175   *shading; Culberg et al., 2021) detections along OIB flight lines (black interior lines); and AR radargram*
1176   *transect A-B (red line; Fig. 3a), and C-D (orange line; Fig. 3b).*
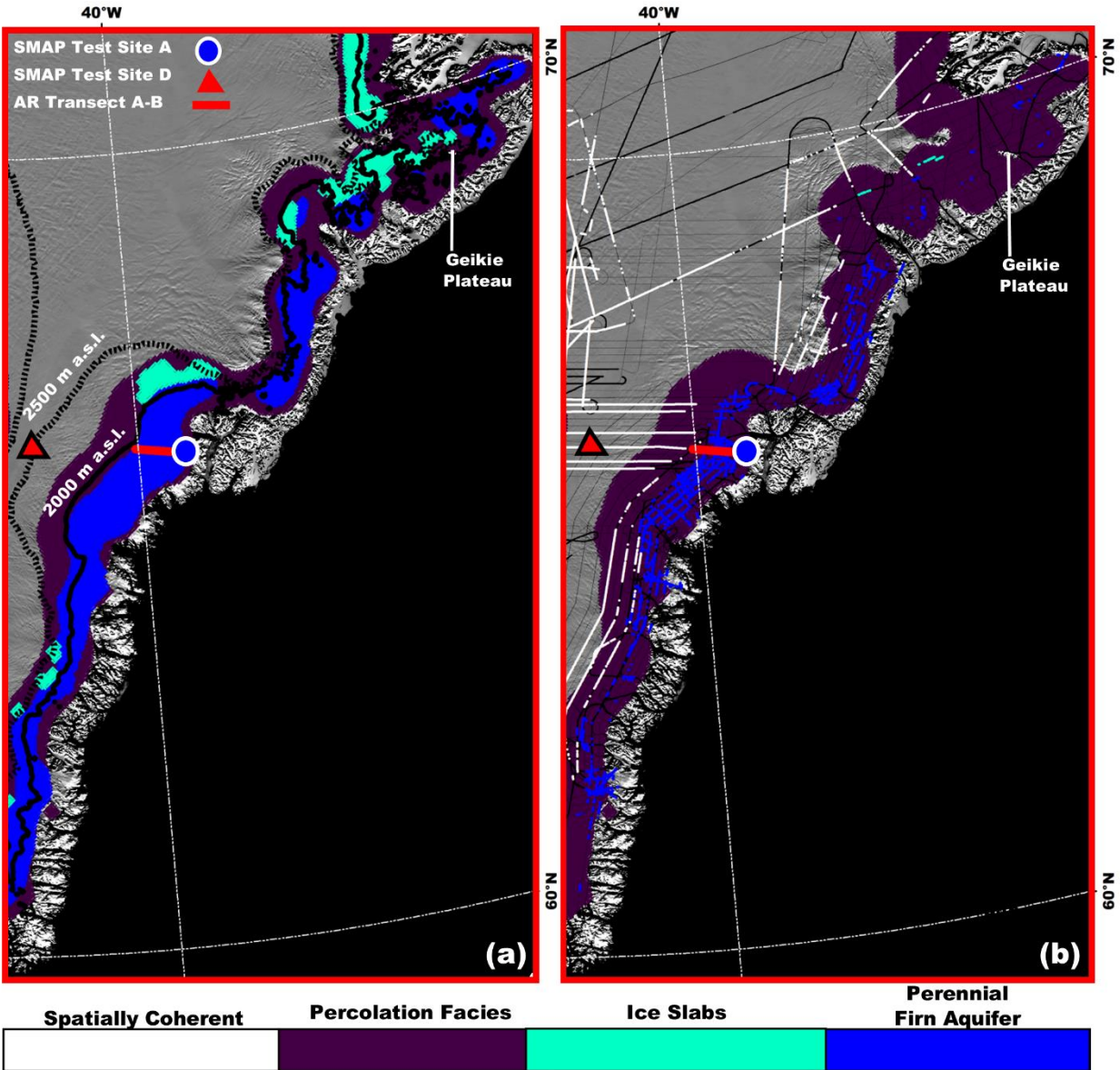
Figure 8

The SMAP-derived perennial firn aquifer (blue shading), ice slab (cyan shading), and percolation facies (purple shading) extents (2015-2019) generated by the adapted empirical algorithm over south eastern Greenland (red box; Fig. 1c); and the 2000 m a.s.l. contour (black line), and the 2500 m a.s.l. contour (black dotted line; Howat et al., 2014) overlaid on the 2015 MODIS MOG image map (Haran et al., 2018). (b) The SMAP-derived percolation facies extent is overlaid with AR- and MCoRDS-derived 2010-2017 perennial firn aquifer (blue shading; Miège et al., 2016), 2010-2014 ice slab (cyan shading; MacFerrin et al., 2019), and 2012 spatially coherent melt layer (white shading; Culberg et al., 2021) detections along OIB flight lines (black lines); AR radargram transect A-B (red line; Fig. 3a); and SMAP Test Site A (blue circle; Fig. 4a), and D (red triangle; Fig 4d).
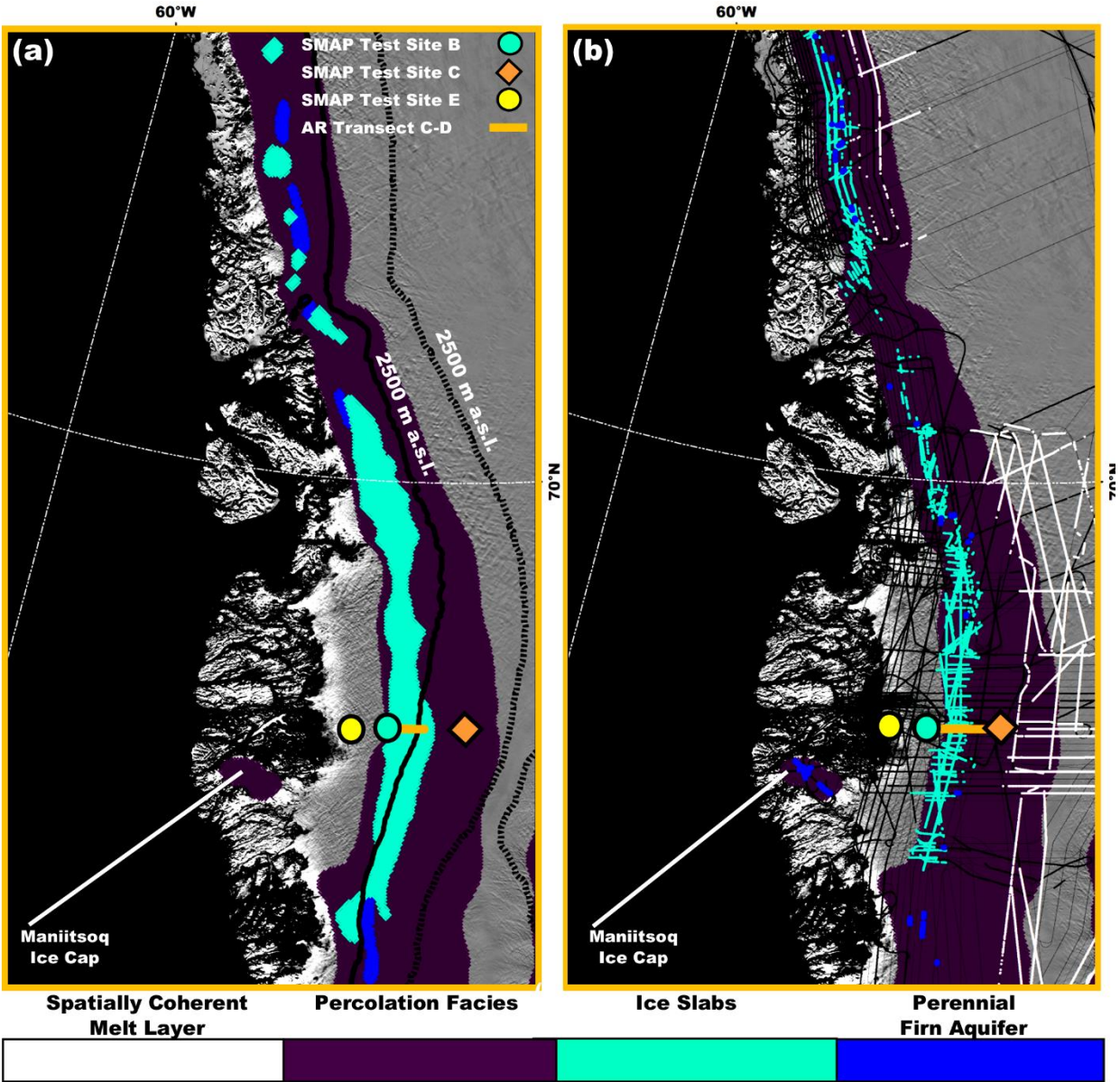
1188

Figure 9

(a) SMAP-derived perennial firn aquifer (blue shading), ice slab (cyan shading), and percolation facies
(purple shading) extents (2015-2019) generated by the adapted empirical algorithm over south western
Greenland (orange box; Fig. 1c); and the 2000 m a.s.l. contour (black line), and the 2500 m a.s.l. contour
(black dotted line; Howat et al., 2014) overlaid on the 2015 MODIS MOG image map (Haran et al., 2018).
(b) SMAP-derived percolation facies extent is overlaid with AR- and MCoRDS-derived 2010-2017 perennial
firn aquifer (blue shading; Miège et al., 2016), 2010-2014 ice slab (cyan shading; MacFerrin et al., 2019),
and 2012 spatially coherent melt layer (white shading; Culberg et al., 2021) detections along OIB flight lines
(black interior lines); AR radargram transect C-D (orange line; Fig. 3b); and SMAP Test Site B (cyan circle;
Fig. 4b), C (orange diamond; Fig. 4c), and E (yellow circle; Fig. 4e).

1199

1200 **Table 1.**

1201 *MODIS-derived total number of days in the melting and freezing seasons; SMAP-derived maximum*

1202 *vertically-polarized L-band brightness temperature ($T_{V,max}^B$); minimum vertically-polarized L-band brightness*

1203 *temperature ($T_{V,min}^B$); time scale scales of exponential decrease following the surface freeze-up date for*

1204 *perennial firn aquifer, ice slab, percolation facies, dry snow facies, and wet snow facies areas.*

	Melting Season (days)	Freezing Season (days)	$T_{V,max}^B$ (K)	$T_{V,min}^B$ (K)	Exponential Decrease (time scale)
Perennial Firn Aquifers	75 - 100	265 - 290	200 - 275	180 – 250	weeks – months
Ice Slabs	60 -90	275 - 305	170 - 260	130 – 240	days - weeks
Percolation Facies	1 - 60	305 - 364	150 - 200	130 – 220	days
Dry Snow Facies	-	365	200 - 240	200 – 240	-
Wet Snow Facies	90 - 120	245 - 275	230 - 250	230 – 250	-

1205

1206 **Table 2.**

1207 *SMAP-derived calibration parameter intervals used for mapping perennial firn aquifer and ice slab extents.*

	ξ	$T_{V,max}^{B}$ (K)	$T_{V,min}^{B}$ (K)	ζ
Perennial Firn Aquifers	0.2 – 2.8	200 – 275	180 – 250	-0.04 – -0.02
Ice Slabs	0.1 – 2	170 – 260	130 – 240	-0.06 – -0.03

1208

 Table 3.

1210 *Interannual variability in SMAP-derived perennial firn aquifer and ice slab extents.*

	Perennial Firn Aquifers (km^2)	Ice Slabs (km^2)
2015-2019	66,000	76,000
2015-2016	63,000	23,000
2016-2017	69,000	48,000
2017-2018	73,000	27,000
2018-2019	70,000	38,000

1211